LJMU Research Online

Callingham, TM, Cautun, M, Deason, AJ, Frenk, CS, Grand, RJJ, Marinacci, F and Pakmor, R

 The orbital phase space of contracted dark matter haloes

Article

For more information please contact researchonline@ljmu.ac.uk

The orbital phase space of contracted dark matter haloes

Thomas M. Callingham [ORCID],[1]★ Marius Cautun [ORCID],[2] Alis J. Deason [ORCID],[1] Carlos S. Frenk,[1] Robert J. J. Grand [ORCID],[3] Federico Marinacci [ORCID][4] and Ruediger Pakmor [ORCID][3]

[1]*Institute of Computational Cosmology, Department of Physics, University of Durham, South Road, Durham DH1 3LE, UK*
[2]*Leiden Observatory, Leiden University, P.O. Box 9513, NL-2300 RA Leiden, the Netherlands*
[3]*Max-Planck-Institut für Astrophysik, Karl-Schwarzschild-Str. 1, D-85748 Garching, Germany*
[4]*Department of Physics and Astronomy, University of Bologna, via Gobetti 93/2, I-40129 Bologna, Italy*

ABSTRACT

We study the orbital phase space of dark matter (DM) haloes in the AURIGA suite of cosmological hydrodynamics simulations of Milky Way (MW) analogues. We characterize haloes by their spherical action distribution, $F(J_r, L)$, a function of the specific angular momentum, L, and the radial action, J_r, of the DM particles. By comparing DM-only and hydrodynamical simulations of the same haloes, we investigate the contraction of DM haloes caused by the accumulation of baryons at the centre. We find a small systematic suppression of the radial action in the DM haloes of the hydrodynamical simulations, suggesting that the commonly used adiabatic contraction approximation can result in an underestimate of the density by ~ 8 per cent. We apply an iterative algorithm to contract the AURIGA DM haloes given a baryon density profile and halo mass, recovering the true contracted DM profiles with an accuracy of ~ 15 per cent, that reflects halo-to-halo variation. Using this algorithm, we infer the total mass profile of the MW's contracted DM halo. We derive updated values for the key astrophysical inputs to DM direct detection experiments: the DM density and velocity distribution in the Solar neighbourhood.

Key words: Galaxy: halo – Galaxy: kinematics and dynamics – Galaxy: structure – galaxies: haloes – galaxies: kinematics and dynamics.

1 INTRODUCTION

The past three decades have seen tremendous advances in our understanding of galaxies and the dark matter (DM) haloes in which they form. From a theoretical perspective, much effort has been directed at understanding structure formation in collisionless *N*-body simulations, in which both DM and baryons are modelled as a single dissipationless fluid (see e.g. Zavala & Frenk 2019, for a recent review). These are often referred to as 'dark matter-only' (hereafter DMO) simulations. Such cosmological simulations show that overdense regions first collapse to form small haloes, with larger structures forming hierarchically through mergers of smaller objects and accretion of diffuse mass (Frenk et al. 1988). The resulting DM haloes have universal density profiles that are well fit by the NFW form (Navarro, Frenk & White 1996, 1997):

$$\rho(r) = \frac{\rho_s}{\frac{r}{r_s}\left(1 + \frac{r}{r_s}\right)^2},\qquad(1)$$

which is characterized by two free parameters: the scale radius, r_s, and the characteristic density, ρ_s. The scale radius is related to the size of the halo, R_{200},[1] through the concentration, $c_{200} = R_{200}/r_s$. The origins of this simple profile are still debated, with suggestions including a close connection to the halo merger history or an attractor solution to entropy-driven relaxation (e.g. Pontzen & Governato 2013; Ludlow et al. 2014).

This conformity of haloes in DMO simulations is broken when baryonic physics are included in fully hydrodynamical simulations (hereafter 'Hydro'). Such simulations include many of the physical processes thought to be important in the formation of galaxies, such as gas cooling and heating, stellar winds, chemical evolution, and supernova and active galactic nucleus feedback (e.g. see Somerville & Davé 2015); they thus have a much more complex and rich behaviour than their DMO counterparts. In particular, gas cools and condenses at the halo centre, where it forms stars. This results in DM haloes that have higher central densities than an NFW profile, and that are often referred to as having been 'contracted'. The amount of DM contraction depends on many

---

★ E-mail: thomas.m.callingham@durham.ac.uk

[1]This is defined as the radius within which the mean density is equal to 200 times the critical density.

factors including the mass of the central galaxy, its assembly history and the orbital distribution of DM particles (e.g. Barnes & White 1984; Blumenthal et al. 1986; Gnedin et al. 2004; Abadi et al. 2010; Duffy et al. 2010; Dutton et al. 2016; Schaller et al. 2016; Artale et al. 2019).

DM haloes cannot be observed directly, of course, but some of the properties of the Milky Way (MW) halo can be inferred from observations of tracers of the gravitational potential. The latest *Gaia* data release (DR2, Gaia Collaboration et al. 2018) provides a remarkable data base of full 6D phase-space measurements of stars in the inner regions of the MW. Combined with other data sets, such as SDSS (Abolfathi et al. 2018) and APOGEE (Majewski et al. 2017), the *Gaia* data have been used to place tight constraints on the MW's circular velocity curve (Eilers et al. 2019) and local escape velocity (e.g. Deason et al. 2019), and thus have helped constrain the total mass distribution of the MW. The simplest models of the MW assume that the DM halo can be described as an NFW profile. Far from the Galactic Centre, this is a reasonable assumption for the total mass profile (Callingham et al. 2019, hereafter, Callingham19). However, to model the inner regions of our Galaxy it is essential to include the mass distributions of its baryonic components such as the thin and thick discs, the bulge, and the stellar halo (e.g. McMillan 2011, 2017). Previous studies (e.g. Deason et al. 2012; McMillan 2017) have typically found a high halo concentration (∼11–12), which is unusually large compared to the predictions for MW-sized haloes from cosmological simulations (typically ∼8 in the EAGLE cosmological simulation; Schaller et al. 2016). This could be a symptom of the neglect of the contraction of the DM halo and underlines the importance of properly accounting for the changes in the DM distribution induced by the baryonic distribution (e.g. see Cautun et al. 2020).

Several methods have been developed to predict the contracted DM halo profile in the presence of baryons. The simplest are different versions of the adiabatic contraction approximation which assumes that particle orbits are adiabatic invariants (Eggen, Lynden-Bell & Sandage 1962; Barnes & White 1984). An early example of this approach Blumenthal et al. (1986) effectively assumes that all particles are on circular orbits, a rather crude approximation that leads to excessive compression of the orbits. This method was improved by Gnedin et al. (2004), Gnedin et al. (2011), who modified it to take into account that DM particles are typically on non-circular orbits. However, these improved versions neglect the fact that DM particles have a distribution of orbits. Cautun et al. 2020, (hereafter, Cautun20) have studied the contraction of DM density profiles in the EAGLE and AURIGA simulations and derived an analytic prescription for the average halo contraction; their approach is unbiased and recovers the profiles of DM haloes in hydro simulations with an accuracy of ∼ 10 per cent that reflects the halo-to-halo scatter.

While these methods are easy to apply, they neglect important information and provide only limited understanding. To model the effects of contraction properly it is necessary to consider the complex dynamics within the DM halo. While often viewed as static profiles, haloes are made up of particles moving on various orbits (Zhu et al. 2017) that conspire to give a steady density profile. For a halo in equilibrium it follows from the Jeans theorem that the distribution of the DM particles is solely dependent on integrals of motion (IoM), with no dependence on phase. The halo can therefore be described as a collection of orbits defined by IoM instead of particles. The natural choice for this description are the action integrals $[J_i]_{i = 1, 2, 3}$. One significant advantage that the actions have over other IoM is that they are adiabatic invariants, and thus largely

unchanged by sufficiently slow changes in the potential (Binney & Tremaine 1987).

The distribution function (DF) of DM particle actions, $F(J)$, can be thought of as an orbital blueprint of DM haloes that may be use to calculate various halo properties, such as the density and velocity anisotropy profiles. If the growth of the baryonic component is a slow, adiabatic process, then the DM halo is described by the same $F(J)$ as in the absence of baryons, that is as in DMO simulations. Given this adiabatic assumption, the differences between haloes in DMO and Hydro simulations is induced solely by the deeper gravitational potential of the baryons which are more centrally concentrated in the Hydro than in the DMO simulations. While the haloes are composed of DM particles on orbits with the same J values, the deeper potential compresses the DM orbits to lower radii in physical space, resulting in a higher central density in the Hydro simulations.

The extent to which the adiabatic assumption holds is unclear and depends on the time-scale on which the baryons cool and accumulate at the centre. If the cooling time-scale is shorter than the free-fall time-scale, then the gas undergoes rapid cooling, a non-adiabatic process. Alternatively, if the cooling time-scale is much larger than the free-fall time-scale, the growth of the baryonic component is adiabatic. There is evidence from analytic arguments (White & Frenk 1991) and simulations (e.g. Correa et al. 2018) that the MW-mass haloes are in the slow cooling regime. Once the baryons have settled in the centre of the halo in a quasi-hydrostatic state they dominate the central gravitational potential. Subsequent violent events, such as gas blowouts, can change the inner mass profile rapidly over short time-scales, transferring energy to DM particles in the central region of haloes. For haloes that host dwarf galaxies, this process could form cores in their DM distribution (e.g. Navarro et al. 1996; Pontzen & Governato 2012; Benitez-Llambay et al. 2018; Burger & Zavala 2019).

To perform action angle modelling, it is necessary to chose a specific DM action DF, $F(J)$. Typically and, in particular, for isolated DMO haloes, the DF is derived analytically, often assuming that the DM particle orbits have an isotropic velocity distribution. Under the adiabatic assumption, these orbits can then be combined with a given baryon potential to construct a contracted DM halo. This approach was tested by Sellwood & McGaugh (2005) against *N*-body simulations that included a slowly grown analytic baryonic component. By using simple action DFs, Sellwood and McGaugh found that radially biased haloes resist compression, while isotropic distributions end up more compressed (in agreement with the results of Gnedin et al. 2004). In the past decade, there have been significant technical advances in the numerical calculation of action angles and in the overall modelling framework (Vasiliev 2019). More complex action DFs, including one that produces an approximate NFW density profile in isolation, were analytically derived by Posti et al. (2015) and used in a series of papers of increasing complexity, in which the MW is modelled with multiple baryon components (Piffl, Penoyre & Binney 2015; Binney & Piffl 2015). In the most recent study, by Cole & Binney (2017), the DF of Posti et al. was modified assuming a non-adiabatic, baryon-driven upscattering of low action orbits, generating a cored DM profile.

Action angle modelling of haloes is frustrated by the lack of a standard NFW action distribution; currently there is no well established $F(J)$ model that has been rigorously tested in cosmological simulations. The scatter in DM halo properties, such as concentration and velocity anisotropy (Navarro et al. 2010), adds further complexity to the task of parametrizing a general action DF of a DM halo. This scatter likely causes haloes described

by different DFs to undergo different amounts of contraction for a given baryonic profile; it is therefore important to capture the variation with an accurate and flexible parametrization of the DF. An alternative approach is to use DFs that are directly measured in simulations, especially given the recent increase in the resolution and number of zoom-in simulations of MW-mass haloes (e.g. Fattahi et al. 2016; Sawala et al. 2016; Grand et al. 2017; Garrison-Kimmel et al. 2019).

In this paper, we determine the DF, $F(\boldsymbol{J})$, of DM haloes from the AURIGA simulation suite. This allows us to infer accurate DM DFs and, at the same time, sample the breadth of halo-to-halo scatter in cosmologically representative samples of MW-mass haloes. Each simulation volume has a DMO and a Hydro simulation. By comparing the haloes in one to their counterparts in the other, we can investigate the validity of the *ansatz* that the formation of MW-like galaxies is an adiabatic process. To do so, we first discuss how a halo's density and velocity profiles can be inferred from the action DF, and then test if the halo in the Hydro simulation (hereafter, Hydro halo) can be recovered by adiabatically contracting the DF measured in the corresponding DMO simulation (hereafter, DMO halo).

We illustrate the usefulness of modelling DM haloes with an action DF by a few applications targeted at our Galaxy. Our approach has implications beyond the mass profile since it provides accurate predictions for the DM velocity distribution and its moments. Since we use the observed baryonic component of the MW, these predictions are specific to our Galaxy and unmatched by conventional approaches. We illustrate this by predicting the density and velocity distribution function (VDF) of DM particles in the Solar neighbourhood, key inputs for direct DM detection experiments (Green 2010, 2017). In the literature, the VDF is usually given by the standard halo model (SHM), a isothermal DM mass distribution with a Gaussian VDF; however, high-resolution *N*-body simulations indicate a somewhat different VDF (Vogelsberger et al. 2009). In principle, there is a variety of possible DM DFs, which, in turn, would result in a variety of VDFs at the Solar neighbourhood (e.g. Mao et al. 2013). The sizeable sample of halo DFs that we can measure in the AURIGA simulation suite allows us to characterize the dispersion in the predicted VDF at the Sun's location, and thus quantify some of the uncertainties in direct DM detection experiments.

The structure of the paper is as follows. In Section 2, we introduce our sample of haloes and compare physical profiles and orbital distributions in the DMO and Hydro cases. In Section 3, we construct individual orbits, investigate the effects of compression and develop an iterative method for constructing and contracting physical haloes. We apply this to haloes in our sample and study the effects of adiabatic contraction in general. In Section 4, we contract our halo sample according to the MW baryon distribution and present our main results, including predictions for the properties of the MW's local DM distribution. Finally, in Section 5 we summarize our main conclusions.

2 SIMULATED HALOES

In this paper, we use a sample of haloes from the AURIGA project, a suite of 30 high-resolution cosmological zoom-in simulations of individual MW-like haloes (Grand et al. 2017) with halo masses between 1–$2 \times 10^{12} M_\odot$. The haloes were selected from the 100^3 Mpc^3 periodic cube of the EAGLE project, a Λ-cold dark matter (ΛCDM) cosmological hydrodynamical simulation (Schaye et al. 2015). Using the *N*-body and moving mesh magnetohydronymic (MHD)

AREPO code (Springel 2011), these haloes were resimulated to produce both a dark-matter-only and a full hydrodynamic (hereafter referred to as DMO and Hydro respectively) zoom-in simulation of each halo. We primarily use the level 4 resolution sample of 30 haloes, which we label as Au1–Au30. The haloes in the Hydro simulations have a DM particle mass of $\sim 3 \times 10^5 M_\odot$ and an initial gas resolution element of mass $\sim 5 \times 10^4 M_\odot$. For the DMO simulations, the particle mass is $\sim 3.5 \times 10^5 M_\odot$. Both the DMO and Hydro simulations assume the Planck1 (Planck Collaboration XVI 2014) cosmological parameters.

In our analysis, we treat the haloes as being in near spherical equilibrium. In reality, no halo perfectly satisfies this criterium and haloes are often out of equilibrium after following minor or major mergers, before relaxing to equilibrium. To characterize the dynamical state of a halo, we employ the Neto et al. (2007) criteria according to which a halo is relaxed if:

(i) The total mass of substructure within R_{200} is less than 10 per cent of the total halo mass, M_{200}.

(ii) The distance between the centre of mass and the centre of potential of the halo is less than $0.07 R_{200}$.

(iii) The virial ratio $2T/|U| < 1.35$, where T is the total kinetic energy and U the gravitational potential energy of DM particles within R_{200}.

These criteria identify 13 out of the 30 AURIGA haloes as unrelaxed in either the Hydro or the DMO simulations. These haloes are included in our sample in order to investigate the dependence and sensitivity of our analysis to departures from equilibrium. Typically, the haloes relax from the inside out, and the halo outskirts (approximately around and beyond R_{200}) are the least virialized and phase mixed regions. We have checked that most of the relaxed AURIGA haloes are reasonably spherical, especially in the inner regions. For example, the DM particles within $R_{200}/2$ are characterized by the moment of inertia with minor-to-major axes ratio, c/a, of $0.76^{+0.08}_{-0.03}$ in the DMO simulations and $0.87^{+0.03}_{-0.06}$ in the Hydro simulations. The presence of baryons in the Hydro simulations systematically leads to the formation of more spherical haloes, as shown by earlier studies (e.g. Abadi et al. 2010; Zhu et al. 2016; Prada et al. 2019). Throughout this work, we have checked that there are no systematic trends that correlate with the degree of halo asphericity, which suggests that our spherical dynamics treatment represents a reasonable approximation.

While not explicitly shown, we have performed the same analysis on the six AURIGA haloes that were simulated at 8 times better mass resolution than the level 4 simulations considered. While the baryon profiles can differ due to the dependence of subgrid physics on resolution and due to stochastic effects, we find the same results as for the level 4 simulations. As such, we have chosen to show the results obtained using the larger level 4 simulation sample to better characterize the halo-to-halo variability.

2.1 Halo properties

We fit NFW profiles to the spherically averaged DM density profile of our haloes using least-squares fitting in $\log r$ within the range $R_{200}/100 < r < R_{200}$. We find that the NFW profile provides a good fit to the DMO haloes, especially the relaxed ones; however it provides a poorer description of the DM distribution in the Hydro simulations (see also e.g. Schaller et al. 2016; Cautun et al. 2020). None the less, for completeness we calculate the best-fitting NFW profile for the DM haloes in the Hydro simulation as well. In this case, because of the poor fits, the inferred scale radius and concentration
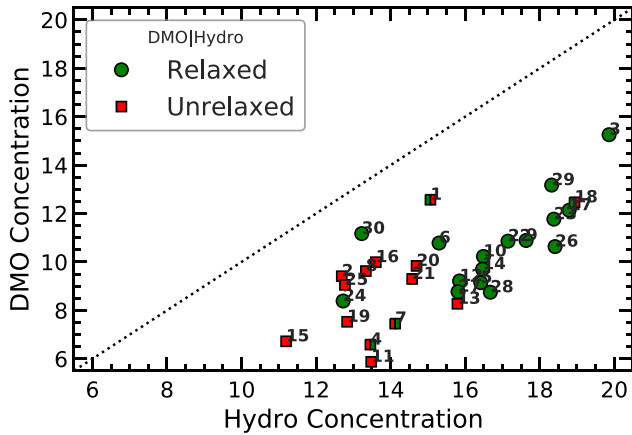
Figure 1. The concentrations, $c_{200} = R_{200}/r_s$, of the 30 AURIGA haloes in the DMO and Hydro simulations, obtained by fitting an NFW profile to the DM distribution in each case. The points are green circles or red squares if the haloes are relaxed or unrelaxed. The contraction of the DM haloes in the Hydro simulations increases their concentration relative to the DMO case.

can strongly depend on the radial range used for the fitting. The resulting concentrations of the DMO and Hydro haloes are shown in Fig 1. The concentration of the Hydro haloes is systematically higher, indicating an increase in DM density in the inner regions. It can also be seen that unrelaxed haloes typically have slightly lower concentration, in agreement with previous studies (Neto et al. 2007).

The effects of contraction may be seen in more detail by comparing the spherically averaged profiles of a halo in the DMO and Hydro simulations. This is shown in Fig. 2, which presents the shell mass, $M_{\rm Shell} = 4\pi r^2 \rho$, the velocity dispersion, σ_V, and the velocity anisotropy, $\beta = 1 - \sigma_T^2/\sigma_r^2$ (where σ_t and σ_r represent the tangential and radial velocity dispersions, respectively) for one of the relaxed haloes, AU5. The DMO density is scaled by $1 - f_{\rm Baryon}$ to subtract the cosmic baryon fraction, $f_{\rm Baryon} = \Omega_{\rm Baryon}/\Omega_{\rm Matter}$. As expected, the DMO halo density (top panel) is well fitted by the NFW form, with the best-fitting NFW profile shown by the red solid curve. The velocity dispersion (top middle panel) of the DMO halo peaks just inside the scale radius, which corresponds to the maximum of $M_{\rm Shell}$. The density at each radius can be interpreted as a measure of the number of different orbits at that radius, so the peak at the scale radius reflects the relatively higher number of orbits that pass through this radius. The velocity anisotropy, $\beta^{\rm DMO}(r)$, is nearly isotropic in the centre and becomes more radially biased towards the outskirts, again in agreement with previous studies (Tissera et al. 2010; Navarro et al. 2010). While all of our relaxed DMO haloes conform to the NFW form, we see significant scatter in their concentrations and variations in their velocity dispersion and velocity anisotropy.

For the Hydro halo, we find a DM profile that is more centrally concentrated (orange line in the top panel of Fig. 2). This is due to response of the halo to the baryonic distribution (green line), which is much more centrally concentrated than in the DMO simulation (in which, by construction, the 'baryons' have the same profile as the DM, but with a different normalization). The baryons deepen the central potential, compressing the orbits of the DM particles inwards and significantly increasing the DM density and total velocity dispersion in the central regions. The velocity anisotropy, β, profile varies only slightly between the DMO and Hydro haloes, with the DMO haloes typically having a slightly more radially
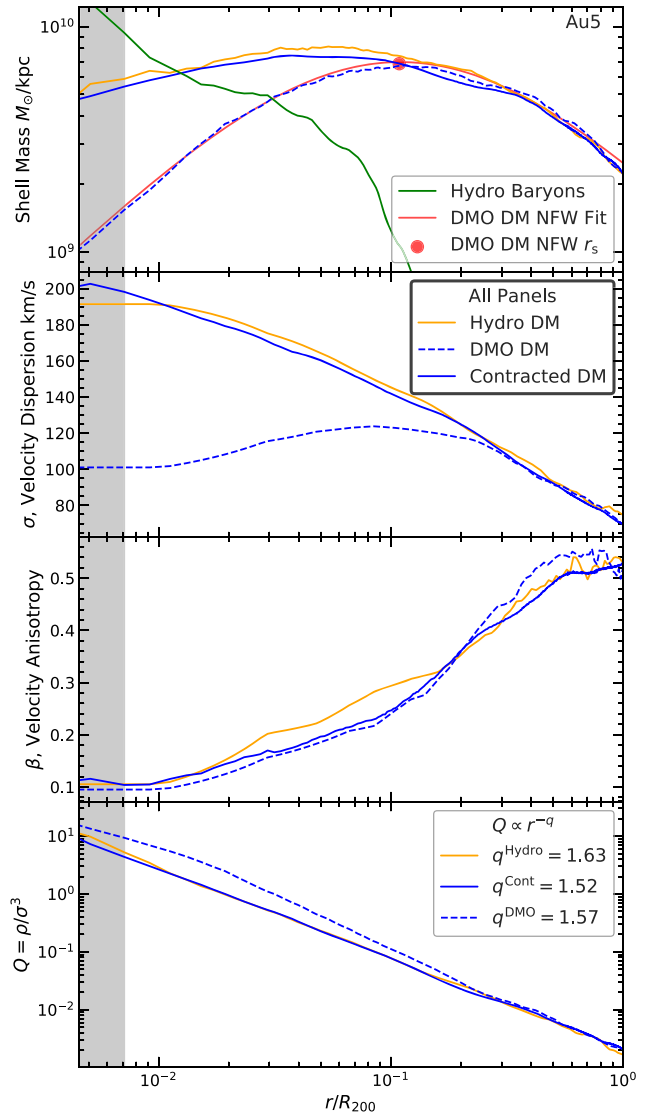

Figure 2. An illustration of the density, velocity dispersion, and velocity anisotropy profiles of a DM halo (AURIGA halo 5) shown for the DMO (dashed blue) and the Hydro (solid orange) versions of the simulation. Compared to the DMO case, the Hydro halo has a higher density in the central regions (top panel), along with an increased velocity dispersion (second panel). The third panel shows only small differences in the velocity anisotropy, β. The bottom panel shows the pseudo-phase-space density, $Q(r) = \rho/\sigma^3$, which we find is well fitted by a simple power law for both DMO and Hydro haloes. Also plotted is the contracted DMO halo (solid blue), which was obtained by applying the method described in Section 3.1. This closely reproduces the Hydro halo. The grey shaded region corresponds to r values below the convergence radius of the simulation (Power et al. 2003).

biased velocity anisotropy between the scale radius and R_{200} (this is not the case for the AU5 halo shown in Fig. 2), but there is significant halo-to-halo scatter.

The bottom panel of Fig. 2 shows the so-called peudo-phase-space density, $Q(r) = \rho/\sigma^3$. Surprisingly, in DMO haloes this quantity has been shown to closely follow a simple power law, $Q \propto r^{-q}$, with a theoretically predicted slope, $q \sim 1.875$ (Bertschinger 1985), that is consistent with our results, $q \sim 1.84^{+0.04}_{-0.07}$. The origin of this relation remains unclear, and whether it is a fundamental feature or

a dynamical 'fluke' is debated in the literature (e.g. Ludlow et al. 2010; Navarro et al. 2010; Ludlow et al. 2011; Arora & Williams 2019). We find that the Hydro haloes also conform to this power law (in agreement with Tissera et al. 2010), with similar scatter but with a shallower slope $Q_{\mathrm{Baryon}} \sim 1.62^{+0.08}_{-0.08}$. We leave this interesting observation for future work.

2.2 Orbital phase space

As we discussed in the Introduction, we are interested in describing DM haloes in terms of their action distribution, $F(\boldsymbol{J})$. This provides a complete description of the orbits of particles in the halo, which can be used as the blueprint to reconstruct various halo properties, as we shall see in the next section.

We model haloes as spherically symmetric distributions for which the gravitational potential, $\Phi(r)$, is related to the total density profile, $\rho(r)$, by:

$$\Phi(r) = -4\pi G \left(\frac{1}{r} \int_0^r r'^2 \rho(r') \, dr' + \int_r^\infty r' \rho(r') \, dr' \right), \quad (2)$$

where G is Newton's gravitational constant. Spherical symmetry reduces the number of actions needed to describe each orbit to two as the third action is identically zero and the orbit stays in a plane between its pericentre, r_{min}, and apocentre, r_{max}.

The two non-zero actions are the specific angular momentum, L, and the radial action, J_r, given by:

$$L = |\boldsymbol{r} \times \boldsymbol{v}| = r v_{\mathrm{t}}$$
$$J_{\mathrm{r}} = \frac{1}{\pi} \int_{r_{\mathrm{min}}}^{r_{\mathrm{max}}} v_r(r) \, dr \quad (3)$$

An alternative IoM commonly used in dynamical modelling is the (specific) energy, E, defined as:

$$E = \frac{1}{2} |\mathbf{v}|^2 + \Phi(r) \quad (4)$$

While convenient to calculate, E is not an adiabatic invariant. The energy DF, $F(E)$, is therefore expected to differ systematically between the DMO and the Hydro simulations, whereas $F(L)$ and $F(J_{\mathrm{r}})$ are expected to remain approximately the same. Note that in this paper all distributions, F, are normalized to integrate to 1.

Here, the distributions are found for each halo by selecting, from the centre outwards, the same number of DM particles for each DMO and Hydro counterpart halo, contained within R_{200} of the Hydro halo. In general, haloes in the DMO and Hydro simulations are well matched. However, the stochastic nature of galaxy formation, as well as the small inherent numerical effects, cause small differences in the distributions of DM particles. On average, we find that ~ 90 per cent of the DM particles within R_{200} in the Hydro case are also found within R_{200} in the DMO case. We have checked that differences in the haloes' orbital distributions discussed in this study are not caused by unmatched DM particles between the Hydro and DMO cases; distributions of matched particles differ by similar amounts.

To compare the distributions of different mass haloes, the IoMs (of both the Hydro and DMO haloes) are rescaled to give values that are independent of the host halo mass (see Zhu et al. 2016; Callingham et al. 2019). The actions, L and J_r, are normalized by the characteristic angular momentum of a circular orbit at R_{200}, $L_{\mathrm{h}} = \sqrt{G M_{200} R_{200}}$. The energy is similarly normalized by this orbit's energy, $E_{\mathrm{h}} = G M_{200}/R_{200}$.

In Fig. 3, the distributions of L, J_{r}, and E for one example halo (AU5) are shown in the top subpanels. The lower subpanels show the
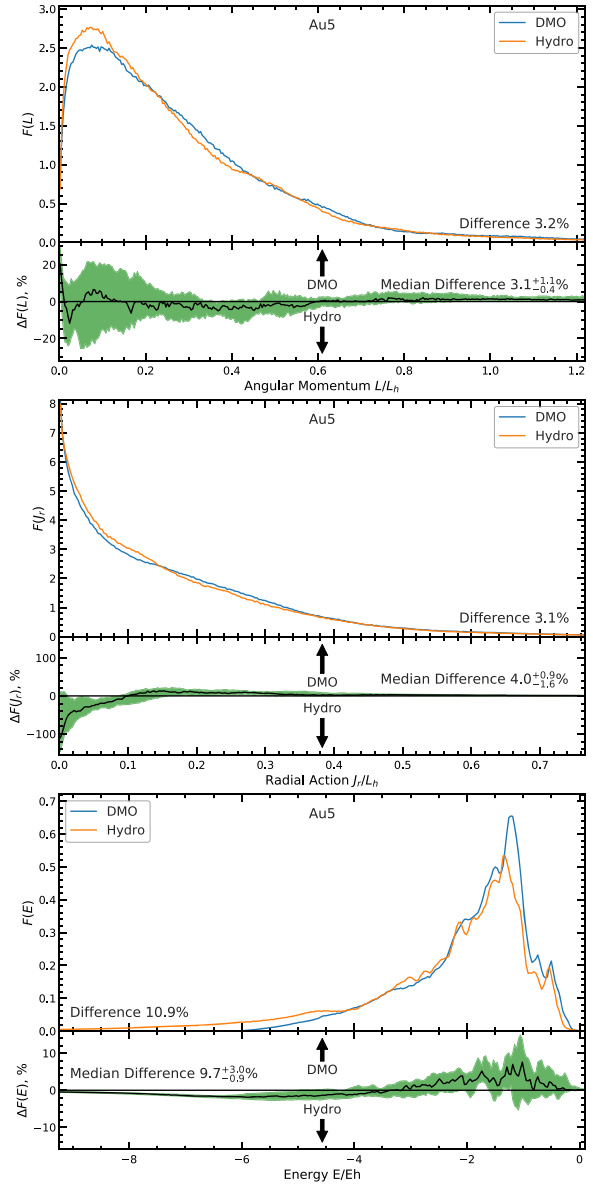

Figure 3. The distributions of angular momentum, L, radial action, J_{r}, and energy, E, of the DM particles in the Hydro and DMO simulations for an example relaxed halo, AU5 (top subpanels). In general, we find small differences between the DFs of the adiabatic invariant actions, $F(L)$ and $F(J_{\mathrm{r}})$, in the DMO and Hydro cases. The distribution of the non-adiabatic invariant energy, $F(E)$, shows larger differences. To check if these differences are systematic, the bottom subpanels show the median (black solid line) and 68 percentiles (green shaded region) of the difference between the DMO and Hydro distributions, $\Delta F = F_{\mathrm{DMO}} - F_{\mathrm{Hydro}}$, for all relaxed AURIGA haloes. To compare different haloes, the orbital values are scaled to be independent of halo mass (for further details, see the main text). The DM energy distributions (bottom panel) are most affected by the presence of baryons, with about 10 per cent of the particles changing energy. These are mainly inner DM particles shifting to lower energies in the deeper Hydro potential. The distributions of the actions, L and J_{r}, experience smaller changes, 3 per cent and 4 per cent, respectively.

difference between the distributions in the DMO and Hydro cases, $\Delta F = F_{\mathrm{DMO}} - F_{\mathrm{Hydro}}$, for all of the relaxed level 4 AURIGA haloes; the solid line is the median and the shaded region indicates the 68 percentiles of the distribution. To estimate the difference between

the various distributions, we calculate the overall difference, Δ, which is effectively the fraction of DM particles whose IoM are distributed differently between the Hydro and DMO cases. This is defined as:

$$\Delta_{\rm X} = \frac{1}{2} \int \left| F_{\rm DMO}(X) - F_{\rm Hydro}(X) \right| \, \mathrm{d}X$$
$$\equiv \frac{1}{2} \int |\Delta F(X)| \, \mathrm{d}X, \tag{5}$$

where X denotes the IoM under consideration, either L, J_r, or E. With this normalization, $\Delta_{\rm X} = 1$ when the distributions are completely different.

The distributions $F(L)$ (top panel) and $F(J_{\rm r})$ (middle panel) are similar to those found in previous simulations (Pontzen & Governato 2013). Between the DMO and Hydro simulations, there is a small, seemingly stochastic difference, in angular momentum ($\Delta_L \sim 3$ per cent) at low L. The difference in J_r is also small, $\Delta_{J_r} \sim 4$ per cent, but systematic, with a slight increase towards low $J_{\rm r}$ for the DM particles in the Hydro case. The energy distributions, $F(E)$ (bottom panel), have distinct peaks and features unique to the individual halo that are not present in the other IoM. These are remnants of a complex merger history, with similar features in the counterpart halo. The energy distributions are most affected by contraction with $\Delta_E \sim 10$ per cent as the deeper central potential of the Hydro halo reduces the energy of the inner DM particles.

We saw that the $J_{\rm r}$ and L 1D distributions are roughly conserved between the Hydro and DMO simulations. But what about the joint 2D $F(J_{\rm r}, L)$ distribution? Is it also conserved? This question is relevant since we find correlations between $J_{\rm r}$ and L, as illustrated in the top panel of Fig. 5. These correlations vary between haloes and potentially encode important information about the halo's density and velocity profiles. To find the answer, we calculate the differences in the $F(J_{\rm r}, L)$ distributions between the DMO and Hydro cases; similarly to equation (5), the action difference, $\Delta_{(J_r, L)}$, is defined as:

$$\Delta_{(J_r, L)} = \frac{1}{2} \int \left| F_{\rm DMO}(J_r, L) - F_{\rm Hydro}(J_r, L) \right| \, \mathrm{d}L \mathrm{d}J_r . \tag{6}$$

For relaxed haloes, $\Delta_{(J_r, L)} \sim 8 \pm 1$ per cent. This is larger than the differences in the 1D distributions, but none the less it is still rather small indicating that the joint distribution is roughly invariant too. The value of $\Delta_{(J_r, L)}$ is used in Appendix B to study the extent to which differences in action distribution are related to differences between the contracted DMO haloes and their Hydro counterparts.

Fig. 4 shows the action distributions $F(L)$ and $F(J_{\rm r})$ of our relaxed AURIGA halo sample. While the individual action distributions have qualitatively similar form, differences in the peak of the distributions suggest object-to-object scatter in the DFs, which could arise from different halo formation histories. This is to be expected as NFW profiles fit the majority of haloes very well, but the concentration and $\beta(r)$ profiles vary from halo to halo. We leave the precise characterization of these distributions and a potential concentration parametrization to future work. Here, we investigate the effects of halo-to-halo variation by calculating the contracted DM halo using multiple $F(\boldsymbol{J})$ distributions.

3 CONSTRUCTING THE HALO FROM PARTICLE ORBITS

In the previous section, we calculated the distribution of DM particle orbits as described by their spherical actions distribution, $F(J_{\rm r}, L)$. We now calculate the individual orbits in physical space to find
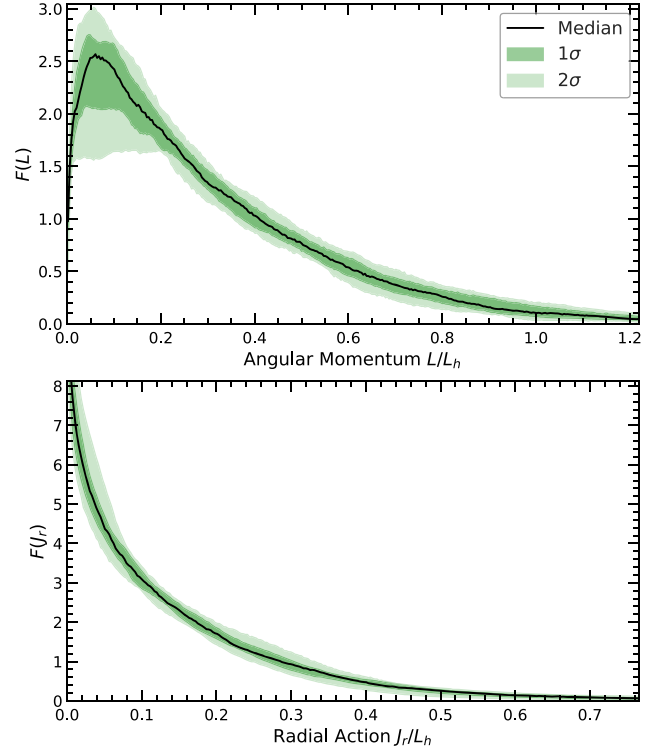

Figure 4. The distributions of angular momentum, L, and radial action, $J_{\rm r}$, of DM particles in the DMO simulation for our sample of relaxed haloes. The black solid line shows the median of our sample and the green shaded region the 68 percentile and full halo-to-halo scatter. To compare haloes, L and $J_{\rm r}$ are scaled to be independent of halo mass (for details, see the main text).

their contribution to the structure of the DM halo. We will use this information in the next subsection where we construct the physical properties of the DM halo, such as its density and velocity dispersion profiles, by summing over the orbital distribution, $F(J_{\rm r}, L)$. Instead of considering a particle as a point contribution to the halo, we consider the physical contribution of its orbit sampled uniformly in phase, that is we consider the contribution of the particle spread around its orbit in time. The radial distribution of an orbit, $F(r|J_{\rm r}, L)$, is defined as the proportion of time that orbit spends at radius r, normalized so that it integrates to unity. This is approximately:

$$F(r|J_{\rm r}, L) \approx \frac{2}{T|_{J_r, L}} \frac{1}{v_r(r)|_{J_r, L}} , \tag{7}$$

where T is the radial time period and v_r is the radial velocity (see Han et al. 2016). However, this is only an approximation and great care is needed at the endpoints where $v_r \to 0$. For a more detailed derivation and further details, please see Appendix A. The density can then be reconstructed by integrating over the distribution of these orbits:

$$\rho(r) = \frac{M_{\rm DM}}{4\pi r^2} \iint F(r|J_{\rm r}, L) \, F(J_{\rm r}, L) \, \mathrm{d}J_r \mathrm{d}L, \tag{8}$$

where $M_{\rm DM}$ is the total mass of the DM halo.

When contracting a DMO halo to account for its baryon distribution, the cosmic baryon fraction must be removed in order to obtain the correct DM halo mass. That is, the mass of the DM halo in the DMO case is given by $(1 - f_{\rm Baryon})$ times the total halo mass. When constructing the halo, $F(J_{\rm r}, L)$ must include all DM particles

within (and orbits calculated up to) $3R_{200}$ to ensure all significant contributions to the halo are included.

In practice, it is simpler first to construct orbits from a given (E, L) pair and a potential, $\Phi(r)$. The $F(E, L)$ distribution is derived from $F(J_r, L)$, given a potential Φ. This can be evaluated numerically using the J_r calculated from each (E, L) pair as:

$$F(E, L) = F(J_r, L) \frac{\mathrm{d}J_r}{\mathrm{d}E}, \quad (9)$$

where $F(J_r, L)$ is evaluated by interpolating the halo action distribution. We can now rewrite equation (8) in terms of the energy and angular momentum distribution to obtain

$$\rho(r) = \frac{M_{\mathrm{DM}}}{4\pi r^2} \iint F(r|E, L) F(E, L) \, \mathrm{d}E \mathrm{d}L. \quad (10)$$

To estimate the DM phase-space distribution, we sample the (E, L) space using a grid of 500^2 orbits. We find that this grid size is a good compromise between computational time and the sufficiently high orbit density needed to recover a smooth halo profile. We have experimented with different methods for defining the (E, L) grid and have selected the one that gives accurate results for the smallest grid size. This is obtained by first choosing 500 L values, evenly spaced in the cumulative $F(L)$ distribution. Then, for each L bin, we select 500 E values evenly spaced on the allowed phase space, that is in the interval $[E_{\mathrm{Circ}}(L), 0]$. By doing so, we neglect unbound particles, i.e. particles with positive total energy, $E > 0$. However, there is only a small fraction of such particles (~ 0.05 per cent; see Fig. 5) and, in practice, excluding them makes no difference.

We illustrate the transformation from (J_r, L) space to (E, L) space in Fig. 5. The top panel shows the distribution, $F(J_r, L)$, of the AU5 halo in the DMO simulation. The bottom two panels show the distribution, $F(E, L)$, for the DMO and Hydro simulations, respectively, which have been calculated from the action DF shown in the top panel using the actual gravitational potential measured in each of the two cases. The $F(E, L)$ distributions are bounded on the lower right edge by circular orbits, which have the minimum energy possible for a given angular momentum. Compared to the DMO case, the Hydro simulation is characterized by more lower energy orbits, a manifestation of the deeper potential well of the Hydro halo.

To gain a better understanding of how a given orbit, (J_r, L), changes between the DMO and Hydro potentials, we select four orbits with the same angular momentum, $L = 0.12L_h$, and increasing radial action, $J_r = [0, 400, 5000, 15000]\,\mathrm{km\,kpc\,s^{-1}}$. These orbits are shown as colour symbols in Fig. 5. The lower the J_r of the orbit, the larger the decrease in energy from the DMO to the Hydro potential, as can be determined from the bottom two panels of Fig. 5.

The change in energy of the orbits between the DMO and Hydro potentials is accompanied by a pronounced change in the radial range associated with a (J_r, L) orbit. This is illustrated in Fig. 6, which shows the fraction of time, $F(r|J_r, L)$, that a particle on orbit (J_r, L) spends at different distances from the halo centre. The figure shows the same four orbits highlighted in Fig. 5. To help interpret the plot, each orbit in Fig. 6 is marked with a triangle symbol, which shows the median radial position of the orbit: a particle spends half its orbital time at farther distances than this. Orbit 1 is circular and lies at the scale radius of the DMO halo. With increasing J_r, the orbits gain radial kinetic energy and become more radial, so their median radial position occurs further out from the circular radius. The orbits spend most of their time at the endpoints, i.e. pericentre and especially apocentre (note the logarithmic y-axis), while they
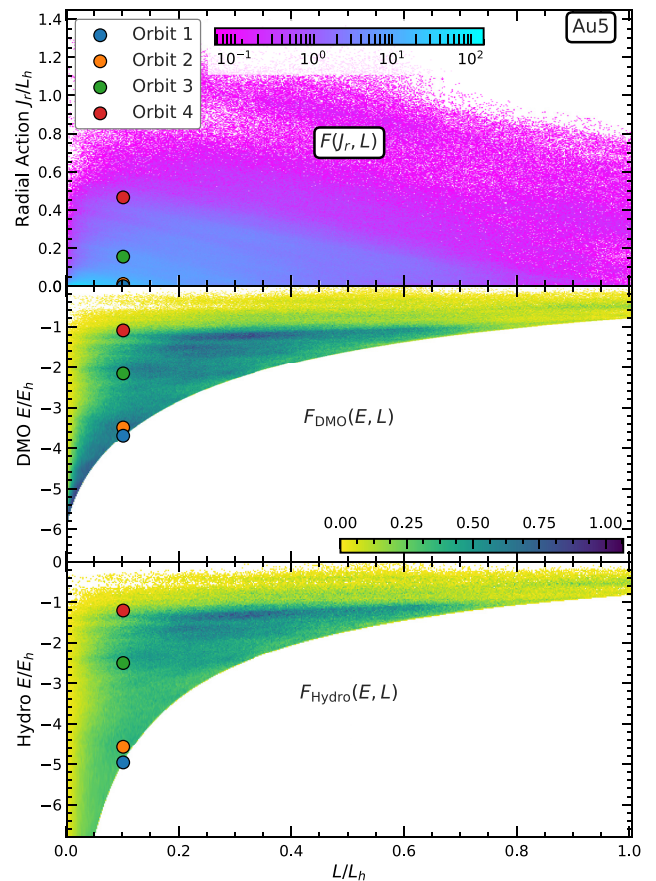

Figure 5. The 2D distribution, $F(J_r, L)$, of radial action, J_r, and angular momentum, L, of the DM particles in the DMO simulation of the AU5 halo (top panel). Given a gravitational potential, $F(J_r, L)$ can be used to calculate the 2D distribution, $F(E, L)$, of energy, E, and L. The result is illustrated in the centre and bottom panels, which show $F(E, L)$ for the DMO and Hydro simulations, respectively. The deeper potential in the Hydro case leads to overall lower energy orbits. To better illustrate the transformation, the colour symbols show four orbits selected to have the same L, but different J_r values. The radial profiles of these orbits are shown in Fig. 6. The actions are given in units of $L_h = \sqrt{GM_{200}}$ and energy in $E_h = GM_{200}/R_{200}$.

spend the least amount of time at the circular radius for their given angular momentum where v_r is maximal.

Adding baryons deepens the potential well and the orbits are pulled inward, leading to a compression of the DM halo. This can be seen by comparing the DMO orbits (dashed lines) with the Hydro ones (solid lines). The more circular orbits are compressed the most, with fractional decreases in the median radius of orbits from 0.7 for Orbit 1 to 0.9 for the most radial Orbit 4. This is agreement with the suggestion that radial orbits 'resist' compression (Sellwood & McGaugh 2005; Gnedin et al. 2004).

3.1 Finding a self-consistent halo

Our aim is to construct a DM halo in physical space, inferring the density and velocity profiles solely from the DM action distribution, $F(J_r, L)$. In the previous section, we showed that given a fixed potential, Φ, we can obtain the DM density profile, $\rho_{\mathrm{DM}}(r)$, from the action DF by calculating the radial distribution, $F(r|J_r, L)$, of individual orbits that is then integrated over $F(J_r, L)$ to obtain the overall radial distribution of DM particles (see equation 8).
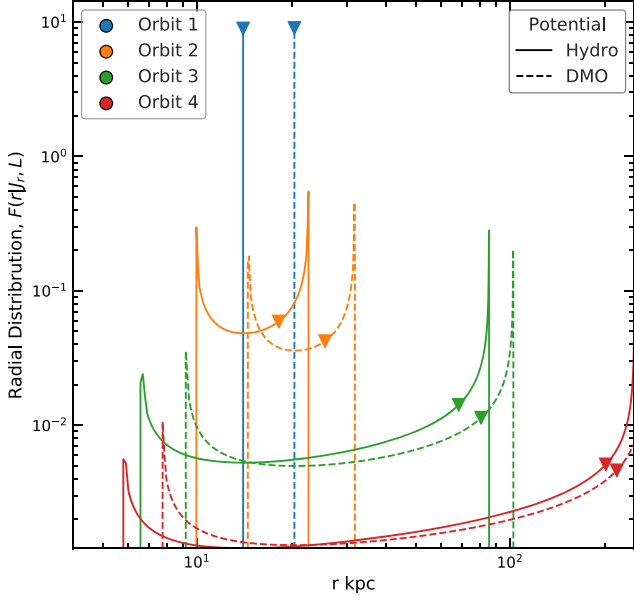
Figure 6. The radial distribution, $F(r|J_r, L)$, for four different orbits (each shown by a different colour). This is equivalently the fraction of time that a particle on orbit (J_r, L) spends at a given radius, per kpc. The orbits have the same angular momentum, L, but increasing radial action, J_r (from Orbit 1 to Orbit 4, where Orbit 1 is circular – see colour symbols in Fig. 5). We show the orbits for the gravitational potential of the AU5 halo in the DMO (dashed lines) and Hydro (solid lines) cases. The triangles show the median radius of each orbit. The deeper Hydro potential pulls the orbits to lower radius, affecting the more circular orbits the most.
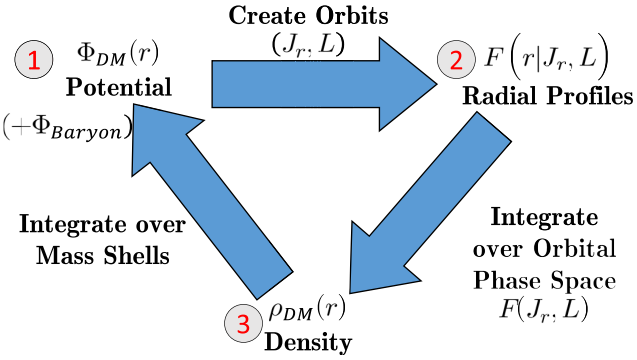

Figure 7. Flowchart of an iterative scheme to calculate a halo density profile starting from its action distribution, $F(J_r, L)$. The method proceeds as follows: (1) using a trial gravitational potential for the DM, Φ_{DM}, calculate the radial range, $F(r|J_r, L)$, of each orbit, (J_r, L); (2) integrate over all orbits to calculate the DM density profile, ρ_{DM}; and (3) use the inferred DM density to update the DM potential, Φ_{DM}; and repeat from step (1) until convergence is achieved. If required, an additional baryon potential Φ_{Baryon} can be added in step (1) to find a contracted halo.

To obtain the true halo density profile we need to know the total gravitational potential, Φ, of the baryonic and DM components. The challenge arises from the fact that the DM gravitational potential needs also to be calculated from the action distribution. Here, we describe how this can be done in a self-consistent way using an iterative approach. We first make an initial guess for the potential which, at each iteration, is updated to a value that is ever closer to the true potential.

Our approach is illustrated in Fig. 7 and proceeds as follows. First a sensible trial potential, Φ_{DM}^0, is chosen, for example, the potential of an NFW halo of average concentration for the target halo mass. When considering the Hydro halo, we typically choose the DM potential from the counterpart DMO halo since this achieves faster convergence. We sum the DM and baryon[2] potentials to obtain the total potential. The DM density is then calculated using equation (8), which, in turn, is used to determine the updated DM potential. This is used as the input potential for the next iteration step, which is repeated until convergence is achieved. The convergence criterion is satisfied when the change in DM density between two iterations is small enough. This is quantified in terms of

$$\Delta_\rho^{\text{total}} = \left(\log \left(\frac{100}{3} \right) \right)^{-1} \int\limits_{R_{200}/100}^{R_{200}/3} \left| \Delta_\rho(r) \right| \, \mathrm{d}\log r \, , \qquad (11)$$

where $\Delta_\rho(r)$ is defined as the fractional difference between two density profiles,

$$\Delta_\rho(r) = 2 \frac{\rho_2(r) - \rho_1(r)}{\rho_2(r) + \rho_1(r)} \, . \qquad (12)$$

The quantity $\Delta_\rho^{\text{total}}$ characterizes the integrated difference between two density profiles in the inner region of the halo, that is for $r \in [\frac{1}{100}, \frac{1}{3}]R_{200}$. When running the iterative approach without a convergence criterion, we find that $\Delta_\rho^{\text{total}}$ reaches a constant small value, $\Delta_\rho^{\text{total}} \in [0.01, 0.005]$ per cent (the exact value varies from halo to halo). The final equilibrium state seems to be reached inside out, with the outskirts of the halo converging somewhat more slowly than the inner parts. Based on this, we choose to stop the iterative procedure to determine the potential when $\Delta_\rho^{\text{total}} < 0.02$ per cent.

We have tested the method by applying it to relaxed AURIGA haloes in both the DMO and Hydro simulations. For example, we measured the $F(J_r, L)$ distribution for a DMO halo, which was then used to recover that halo's density profile starting from an initial potential given by an NFW halo of average concentration for its mass. When compared with the 'true' DM halo profile from the simulation, we find very good agreement: the density is typically recovered to within $\sim$2 per cent within $R_{200}/2$ with increasing scatter of 5 per cent–10 per cent towards the outskirts of the halo. Differences mainly arise from assuming steady state haloes in which particles are uniformly spread in phase along their orbits. However, recently accreted material and substructures do not satisfy this assumption and can lead to differences between the density profile measured in the simulations and that predicted by our method.

3.1.1 Scaling the action distribution to haloes of different masses

In this section, we show how to scale our results from AURIGA haloes to haloes of arbitrary mass. We do this within the context of our method for generating a halo from a given $F(J_r, L)$ distribution. The goal is to take the $F(J_r, L)$ distribution measured for a halo of total mass, M_{200}^{initial}, and rescale it so that it can be used to predict the

---

[2]The baryon potential is kept fixed and is an input to the method, for example the potential from the stellar distribution of an AURIGA halo or of the MW. The method applies to DMO simulations too, in which case the baryon potential is obtained as the cosmic baryon fraction multiplied by the total potential measured in the simulation. The same result is obtained if instead we take a null baryon potential and assume that the DM constitutes 100 per cent of the mass in the DMO simulation.

profile of a target halo with total mass, $M_{200}^{\rm target}$. For this, we exploit the fact that DM haloes, at least in DMO simulations, are universal when scaled appropriately (for more details see the discussion in Li et al. 2017; Callingham et al. 2019). As we saw in Fig. 3, the action distribution for the DMO and Hydro simulations are very similar so we expect the universality to apply to the action distribution not only in the DMO case, but also when including a baryonic component.

As we are interested in matching the total mass of a target halo with a fixed given baryonic profile, we are only free to rescale the mass of the DM halo, not that of the baryonic component. We define the mass scaling factor, $\lambda = M_{200;\,\rm DM}^{\rm target}/M_{200;\,\rm DM}^{\rm initial}$, which is the ratio between the DM mass enclosed within R_{200} for the target and initial haloes, respectively. For DMO haloes, we can rescale the initial halo to the target one by rescaling the positions and velocities by $\lambda^{1/3}$, and the energy and actions by $\lambda^{2/3}$. For Hydro haloes, rescaling the position, velocities, and energy using the same procedure is not a good strategy, especially in the inner halo regions, where the universality of haloes is degraded by the presence of baryons. However, as we discussed earlier, this is not the case for the actions, which scale as in the DMO case.

The rescaled action is given by

$$F'(J_{\rm r}, L) \equiv F^{\rm target}(J_{\rm r}, L)$$
$$= \lambda^{-4/3} F^{\rm initial}\left(J_{\rm r}/\lambda^{2/3}, L/\lambda^{2/3}\right), \qquad (13)$$

where $F^{\rm target}$ and $F^{\rm initial}$ denote the action distribution in the target and original haloes, respectively, and the $\lambda^{-4/3}$ multiplication factor ensures that the new distribution integrates to unity. We then use these new actions, $F'(J_{\rm r}, L)$, as input to the method for constructing the halo density profile described in Section 3.1.

The total mass, $M_{200}^{\rm new}$, of the resulting rescaled halo is close to the target mass, $M_{200}^{\rm target}$, but there can be small differences of order a few per cent. These are present when baryons are included since the baryonic distribution can either contract or expand the DM distribution and thus introduce small variations in the total mass within R_{200}. We account for these small differences by applying again the rescaling method, with the actions now rescaled by a new factor, $\lambda' = M_{200;\,\rm DM}^{\rm target}/M_{200;\,\rm DM}^{\rm new}$, which is typically very close to one. Using the new actions, we calculate again the halo density profile and its total mass, $M_{200}^{\rm new}$, repeating the procedure until convergence to the target halo mass is achieved.

3.2 Contracting AURIGA haloes

We now apply the scheme of Section 3.1 to model the DM haloes in AURIGA. The action distributions of the DM haloes, $F(J_{\rm r}, L)$, as found in Section 2.2, are contracted to a fixed baryon potential, $\Phi_{\rm Baryon}(r)$, taken from the corresponding counterpart halo in the Hydro simulation.

First, we study if the $F(J_{\rm r}, L)$ distribution measured in the DMO simulation can be used to predict the DM distribution in the counterpart Hydro halo. We illustrate this for the AU5 halo in Fig. 2, which shows the DM density as measured for the Hydro halo (orange line) and the contracted DMO halo (blue line). Although there is good overall agreement between the two, the contracted halo density profile is slightly lower than the true one as measured in the Hydro simulation. This systematic difference is consistently seen in all the relaxed AURIGA haloes and is examined further in the top panel of Fig. 8, which shows the fractional difference in density profiles between the contracted DMO and the actual Hydro DM haloes. The contracted halo systematically underpredicts the density profile by ~ 8 per cent over the radial range, $r \in [1/100, 1/3]R_{200}$,
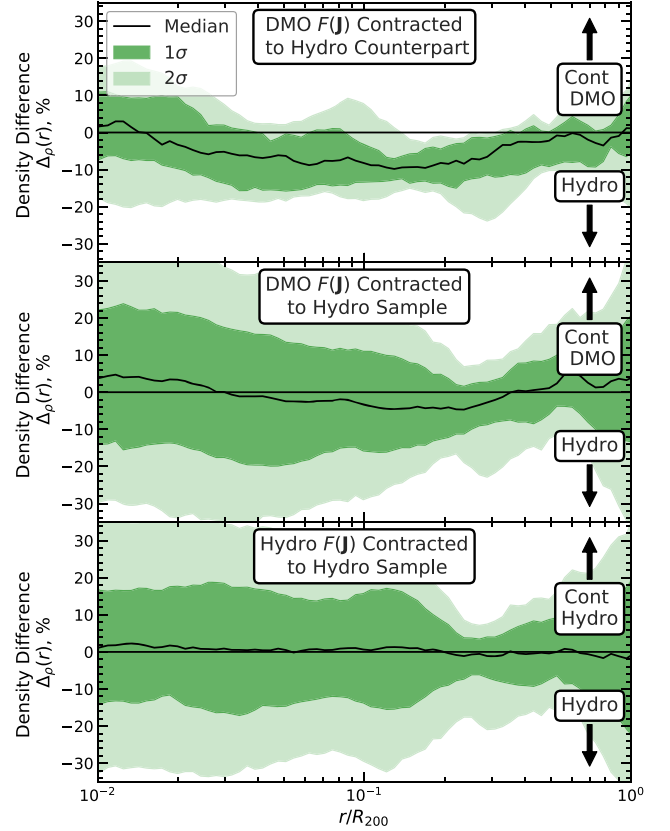

Figure 8. The difference in radial density profiles, $\Delta_\rho(r)$, between DM haloes described by an action distribution, $F(J_{\rm r}, L)$, adiabatically contracted according to a given baryonic profile (see the main text for details) and the 'true' DM haloes in the AURIGA hydrodynamical simulations. We show the results for relaxed haloes only. The black line shows the median and the dark and light green regions indicate the 68 per cent and 95 per cent percentiles, respectively. In the top panel, we compare contracted DMO haloes with their Hydro counterparts, highlighting the effects of unadiabatic differences in the action distributions between the DMO and Hydro simulations on the DM halo density profile. In the middle panel, we contract each DMO halo in turn to every other Hydro halo in the relaxed sample and compare the resulting density profiles, to additionally see the effects of halo variation. In the bottom panel, we contract each Hydro halo in turn to every other Hydro halo across the relaxed sample. This demonstrates the scatter expected when modelling an unknown contracted halo due to halo variation.

while outside this range the agreement is good. This results in M_{200} masses for the contracted haloes that are 5 ± 2 per cent lower than the true masses. This underprediction suggests a systematic, non-adiabatic, difference between the Hydro and DMO action distributions, as we had already encountered in Fig. 3.

To investigate the effects of halo-to-halo variations in action distributions, we contract each of our relaxed DMO haloes in turn according to the baryonic distribution of each relaxed Hydro halo. When doing so, we rescale the actions of the DMO halo to the total mass of each target Hydro halo using the procedure described in Section 3.1.1, ensuring the final contracted haloes have the correct M_{200}. The fractional difference between the density profiles of the contracted and 'true' haloes are shown in the middle panel of Fig. 8. The variation in the DM haloes action distributions, $F(J_{\rm r}, L)$, produces a greater scatter in the contracted density compared to when each halo is matched with its Hydro counterpart. The scatter is largest in the inner third of the halo beyond which the scatter is

noticeably tighter before spreading out again near the outskirts of the halo. This is likely due to the variation in concentration, which mainly effects the inner regions of the halo, $r \lesssim r_s$. Alongside a greater scatter, there is again an underprediction of the contracted density profile, which is slightly reduced by fixing the mass of the contracted haloes to be equal to that of the Hydro haloes.

We can overcome this systematic difference in the predicted density profile by using the DFs measured in the Hydro haloes instead of the DMO haloes, as we have done until now, as shown in the bottom panel of Fig. 8. The resulting contracted DM profiles are unbiased but they have a rather large, ~15 per cent, halo-to-halo variation. This shows that the small systematic differences we have seen in the actions between the DMO and Hydro simulations (see Section 2.2) have measurable effects on the DM density profiles, and that to obtain unbiased contracted DM haloes we need to use the action distribution measured in the Hydro simulations. Thus, to obtain an unbiased model of the MW halo, we need to use Hydro-derived DFs, and, because of system-to-system variations in the DF, we can predict the MW halo density profile only to 15 per cent accuracy.

We have studied in more detail the most important systematic differences between the action DFs in the DMO and Hydro simulations. The tests and the corresponding results are presented in Appendix B. We have found that the small, systematic difference in density profile seen in Fig. 8 is predominantly driven by the suppression of J_r in the Hydro haloes. In the Hydro simulations, some mechanism has caused the DM to lose radial energy in an unadiabatic way. If the systematic decrease of radial action in the Hydro haloes was driven by baryons through either feedback or numerical baryon–DMO particle scattering effects we would perhaps expect to see the strongest effects at the centre of the halo, where the baryon density is highest. However, we see no evidence of a radially varying effect, with the J_r suppression being, on average, approximately the same at all radial distances from the halo centre and at all angular momentum. Furthermore, the feedback-driven cores found in some simulations of dwarf galaxies are formed by increasing the energy of the DM particles, not by reducing it. We leave a more thorough investigation of these non-adiabatic effects to future work.

3.3 Local DM properties in AURIGA

As we discussed in the Introduction, a strength of the halo contraction method presented here is that it can be used to predict all DM halo properties, including the velocity distribution. This is in contrast to most other methods (e.g. Blumenthal et al. 1986; Gnedin et al. 2004; Cautun et al. 2020), which apply only to the halo density profile. In this section, we study how the contraction method can predict dynamical properties of the DM halo, in particular the DM velocity distribution in the Solar neighbourhood, which is a crucial input into DM direct detection experiments. In preparation for modelling the MW in Section 4, we first study the velocity DF (VDF) of the relaxed DM AURIGA haloes. To validate our methodology, we compare the contracted DMO haloes with their Hydro counterparts. Across our sample of different size haloes, we define an AURIGA halo's 'Solar radius' as a set fraction of its R_{200}, $0.036R_{200}$, which was obtained by taking the following MW values: $r_\odot = 8$ kpc and $R_{200}^{MW} \approx 222$ kpc (from Callingham19, corresponding to $M_{200}^{MW} = 1.17 \times 10^{12} M_\odot$).

We illustrate how well our contraction method recovers the DM velocity distribution in the presence of a baryonic component by studying the AU5 halo. Compared to the DMO case, the Hydro halo
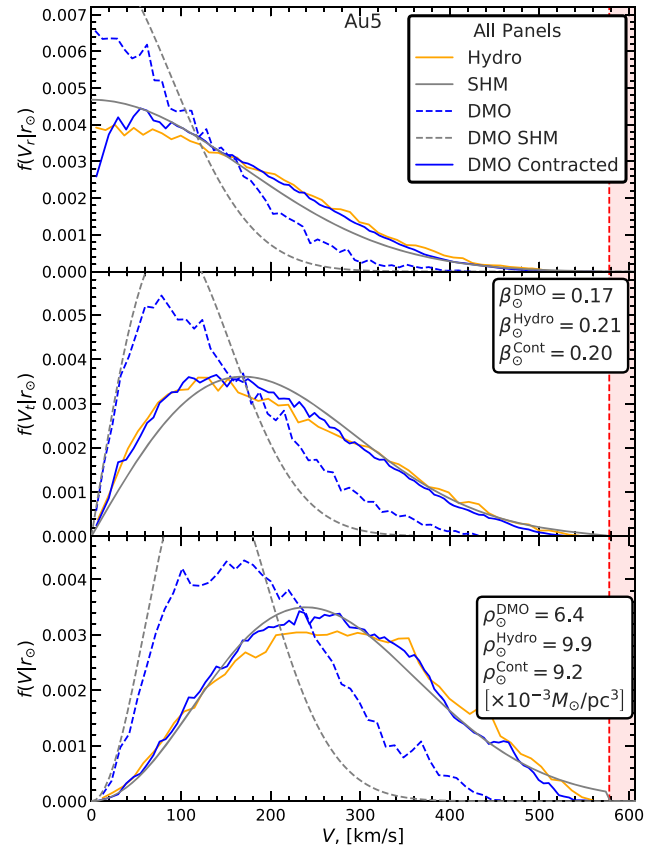

Figure 9. The velocity distributions of DM particles at the Solar neighbourhood in the AU5. The solid orange line shows the distribution measured in the Hydro halo, the dashed blue line shows the corresponding quantity in the DMO case, and the solid blue line in the DMO halo contracted with our method to predict the Hydro quantities. In grey we show the predictions of the SHM, based on the assumption of an isotropic isothermal sphere. The top panel shows radial velocity, v_r, the middle panel tangential velocity, v_t, and the bottom panel total velocity, v. The vertical red shaded region shows velocities larger than the escape velocity of the Hydro halo. Estimates for the Solar neighbourhood DM density, $\rho_\odot$, and velocity anisotropy, $\beta_\odot$ are also given (see the two tables enclosed by a thick black line in the right-hand side of the centre and bottom panels).

has an enhanced density and especially velocity dispersion at the Solar radius, as may be seen in Fig. 2, at the radial position, $r \sim 0.04R_{200}$. The contracted DMO halo reproduces well the Hydro halo, in particular, both the velocity dispersion as well as the velocity anisotropy parameter, β. Thus, our contraction technique reproduces local halo properties that are averaged over many DM particles.

In Fig. 9, we show that the same technique also reproduces the actual DM velocity distribution. For this, we calculate the velocity distribution of all DM particles found within a radial distance of ± 1 kpc around the Solar radius. As expected, the DM particles in the Hydro case are characterized by higher velocities than in the DMO case. The small irregularities in the distribution are the result of the merger history of the halo. The action distribution of the DMO halo can be used to predict the velocity distribution of the contracted DMO halo. This is similar to the approach taken in Section 3.1, where we modelled the density profile. To obtain the VDF, we calculate the velocity components of each $F(r|J_r, L)$ orbit at the solar radius, and then sum over all possible orbits, $F(J_r, L)$ (using

a similar weighting to equation A6). The contracted DMO halo reproduces well the velocity distribution of the Hydro halo, with most differences between the two being stochastic in nature. The only large difference is seen in the radial velocity, v_r, distribution (top panel), where the contracted halo is systematically below the Hydro case for $v_r \rightarrow 0$. This is due to the finite number of orbits included in the reconstruction, with none being exactly at apocentre, pericentre, or on perfectly circular orbits at this radius. This effect is small and can be reduced by including a greater number of orbits in the reconstruction.

The most popular approach in the field is to model the VDF using the SHM (e.g. Evans, O'Hare & McCabe 2019). This is based on the assumption of an isotropic isothermal sphere, and predicts a Gaussian velocity distribution with velocity dispersion, $\sigma = v_{circ}/\sqrt{2}$, which is truncated at the escape velocity, v_{esc}. The SHM predictions for the DMO and Hydro simulations of AU5 are shown in Fig. 9 as dashed and solid grey curves, respectively. The SHM model provides a poor description of the DMO velocity distribution, but performs much better for the Hydro halo. However, we still find important differences between the SHM predictions and the actual Hydro haloes. In particular, the sharp truncation of the SHM VDF at v_{esc} is more abrupt than in the simulations and typically leads to an overprediction of high velocity DM particles. Moreover, the SHM assumes isotropic orbits whereas, in this halo and throughout our sample, we find a small, but non-zero anisotropy parameter at the Solar neighbourhood, $\beta_\odot^{Hydro} = 0.21$. Thus, the isotropic SHM slightly underpredicts the v_r and overpredicts the v_t distributions.

4 APPLICATION TO THE MILKY WAY

We can now apply our DM halo reconstruction method to infer the structure of the DM halo of our own Galaxy. To do this we need to know: the action DF, $F(J_r, L)$, of the MW halo; the MW baryon distribution; and the total mass, M_{200}^{MW}. The last two quantities can be inferred from observations (e.g. Cautun et al. 2020; Wang et al. 2019). For the $F(J_r, L)$ distribution, we assume that the MW is a typical ΛCDM halo and that its DF is similar to that of our relaxed AURIGA haloes. By considering the range of different DFs for the MW, as spanned by the AURIGA haloes, we quantify the extent to which the unknown DM action distribution of our Galactic DM halo affects our predictions. Finally, as we saw in the previous section, there are small systematic differences between the distributions of actions in the DMO and Hydro simulations of MW-mass haloes. Thus, to obtain predictions that are as accurate as possible, we use the $F(J_r, L)$ DFs measured in the Hydro simulations of the AURIGA suite.

We adopt the MW baryon density profile advocated by Cautun20, which we model as a spherically symmetric distribution. Cautun20 assumed parametrized density profiles of a thick and thin stellar disc, a stellar bulge, a cold gas interstellar medium, and an analytically contracted NFW DM halo. Through an MCMC fitting procedure, these baryonic and DM components were fit to the latest MW rotation curve data derived from *Gaia* DR2 (Eilers et al. 2019); the data cover the radial range 5–25 kpc. We also use the total mass of this model, 1.08×10^{12} M$_\odot$, with the final mass of our haloes set through the scheme in Section 3.1.1. This total mass determination is in very good agreement with other measurements based on *Gaia* DR2 (see fig. 5 in Wang et al. 2019), such as the ones based on escape velocity (Deason et al. 2019; Grand et al. 2019), globular cluster dynamics (Posti & Helmi ; Watkins et al.
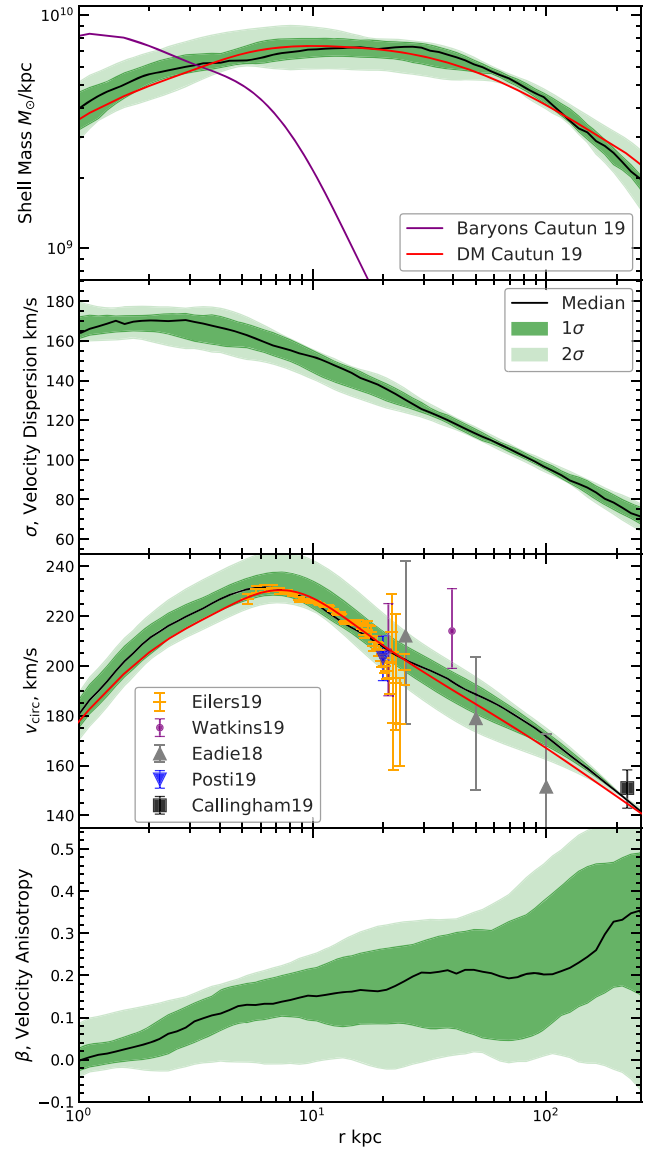

Figure 10. From top to bottom: the MW's density, velocity dispersion, circular velocity, and velocity anisotropy radial profiles predicted by our halo contraction method. The DM haloes are contracted assuming the Cautun20 MW baryonic model and the action distributions, $F(J_r, L)$, from 17 relaxed haloes in the AURIGA Hydro simulations. The black line shows the median prediction of our method, while the dark and light shaded regions show the 68 and 95 percentiles arising from halo-to-halo variation in $F(J_r, L)$. The top panel also shows the Cautun20 baryonic profile (purple) and their best-fitting DM profile (red); the third panel shows in yellow the Eilers et al. (2019) V_{circ} data, and in red the Cautun20 rotation curve for their best-fitting MW model. For comparison to other observational estimates of circular velocity, we include data points from Eadie & Jurić (2019), Watkins et al. (2018), Posti & Helmi (2019), and Callingham et al. (2019).

2018), rotation curve modelling (Cautun20), and satellite dynamics (Callingham19).

Our inferred properties of the MW DM halo are shown in Fig. 10. In the top panel, we see that the median of the contracted density profile closely matches that of Cautun20, although some differences are present. This is to be expected since the Cautun et al. results corresponds to a DM halo that, before baryon contraction, had a concentration of 9.4 , while the 17 AURIGA haloes studied here have

a wide range of concentrations before contraction (averaging 9.7, see Fig. 1). Nonetheless, the Cautun et al. result lies well within the 68 percentile scatter of our predictions, indicating good overall agreement. Not knowing the exact $F(J_r, L)$ distribution of the MW halo results in a ~ 14 per cent scatter (68 percentile range) in the predicted density profile of the contracted halo, in good agreement with our AURIGA results. Our model predicts that the DM velocity dispersion is roughly constant at around 160 km s^{-1} in the inner region of our Galaxy, and then decreases rapidly towards the halo outskirts (second panel in Fig. 10).

In the third panel of Fig. 10, we compare the rotation curve predicted by our model with the actual estimate for the MW as determined by Eilers et al. (2019). We do not fit our model to these data, so the good agreement with observations indicates that our model is making sensible predictions. To compare against the data, we add the rotation curves from both the baryons and the halo. The latter is modelled as a spherically symmetric distribution but for the baryons we need to take into account that their distribution is highly flattened, that is most stars and gas are found in a disc, and that the Eilers et al. rotation curve is measured in the plane of this disc. In the plane of the disc, the true axisymmetric profile gives a $\sim$10 per cent greater contribution to the rotation curve than the spherical profile that we use when modelling the contraction of the DM halo.

The distribution of rotation curves across our contracted DM haloes are in good agreement with both the Eilers et al. data and the Cautun20 best-fitting model. However, we see variation in the curves when using different action DFs. This is to be expected since the MW represents one possible realization of $F(J_r, L)$. It is worth stressing that the median result is not necessarily the 'best' model for the MW DM halo, as the MW is unlikely to reside in a typical ΛCDM halo. Instead, the point to emphasize is that we would expect the MW to lie within the range of our halo sample, thta is within the scatter, which it clearly does. For the data points within 30kpc, we see good agreement with the estimates by Posti & Helmi (2019), Watkins et al. (2018), and Eadie & Jurić (2019). Further out, we find that the Watkins et al. (2018) measurement at 40 kpc lies just outside the 1σ uncertainty of our models, and the lower total mass of Eadie & Jurić (2019) (0.7×10^{12} M$_\odot$) leads to a faster drop off towards R_{200}. Since our total mass is similar, our circular velocity curve matches well that of Callingham19 around R_{200}. For a more detailed discussion see section 6 of Cautun20 which presents a comparison with several other Galactic probes.

While the Eilers et al. circular velocity curve data lie comfortably within the 1σ range of our distribution of contracted haloes, the individual halo curves are poor fits. This shortcoming could be overcome by using the observations to find out which $F(J_r, L)$ distribution best describes the MW data. This can be achieved with an MCMC approach in which we sample different action DFs and concurrently constrain the MW baryonic distribution (e.g. similar to the approach of Cautun20). It is important to marginalize over the MW baryonic distributions, since these are uncertain and, as Cautun20 have shown, there is a degeneracy between the baryon content and the DM halo structure when modelling the MW rotation curve. This approach is beyond the scope of this paper and we leave it for future work.

4.1 MW Local DM distribution

Having inferred the likely structure of the MW DM halo by applying the results of Section 3 based on analysis of 17 AURIGA galactic haloes, we now investigate the implications for the key astrophysical
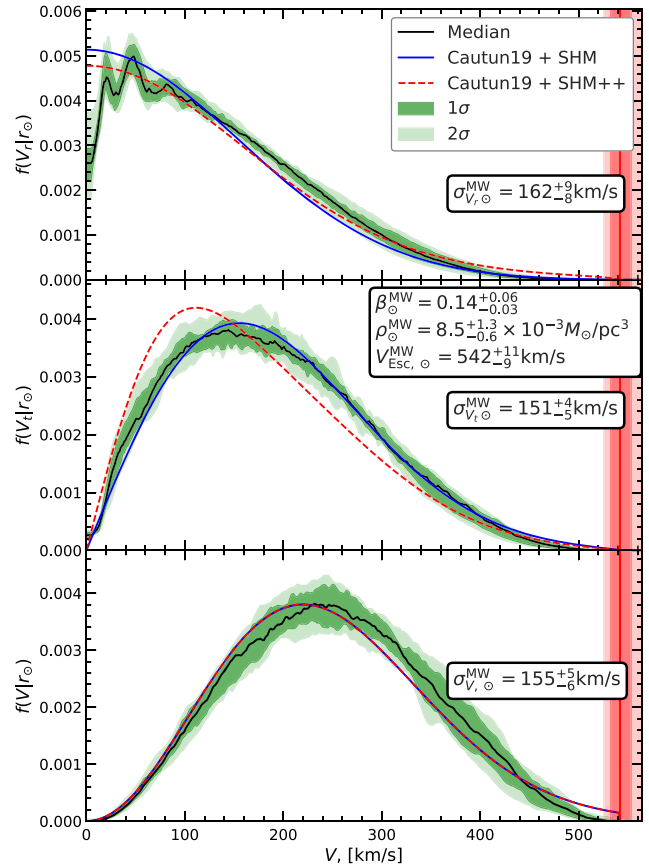

Figure 11. The DM velocity distribution at the Solar radius, $r_\odot = 8$ kpc, as predicted by our halo contraction model. The velocities are with respect to the Galactic Centre. The radial, tangential, and total velocity distributions are shown in the top, middle, and bottom panels, respectively. The median is indicated with a solid black line and the 68 and 95percentiles are shown in shaded green. The blue curve illustrates the velocity distributions given by the SHM and the dashed red curve shows the 'SHM^{++}' variant of Evans et al. (2019), both using $V_{\mathrm{Circ}, \odot}$ and $V_{\mathrm{Esc}, \odot}$ of the Cautun20 MW-mass model. We also give several DM properties at the Solar radius (see the text inserts in the panels) as predicted from our model: the local DM density, $\rho_\odot$; the components of the velocity dispersion, $\sigma_\odot$; the velocity anisotropy, $\beta_\odot$; and the escape velocity, $V_{\mathrm{Esc}, \odot}^{\mathrm{MW}}$ (whose value is also shown as the red shaded region).

inputs to direct DM detection experiments: the density and velocity distribution of the DM in our own solar neighbourhood.

From the DM density profile shown in the top panel of Fig. 10 we find that our models predict $\rho_\odot = 8.5^{+1.3}_{-0.6} \times 10^{-3}$ M$_\odot$ pc^{-3} (equivalently $\rho_\odot = 0.32^{+0.05}_{-0.02}$ GeV^{-1} cm^{-3}). These values are in good agreement with previous estimates (see the compilation by Read 2014). The somewhat large uncertainties in our estimate of $\rho_\odot$ could be significantly reduced if we were to restrict our analysis to those DFs that best fit the MW rotation curve, or individually fit the MW baryon distribution for each DM halo as discussed at the end of the previous section. We find a local speed escape velocity 542^{+11}_{-9} km s^{-1}, which is consistent with the recent *Gaia* DR2 measurements of Deason et al. (2019) and Grand et al. (2019).

In Fig. 11, we highlight the DM velocity distributions at the Solar position predicted by our MW models. These were derived using the method described in Section 3.3 where, for each model, we sum the orbits of all DM particles to find the distribution of radial, tangential and total velocity components. The resulting

Table 1. A list of MW properties in the Solar neighbourhood inferred from our DM halo contraction model. The third and fourth columns give the corresponding values from Cautun20. The velocity dispersion's and anisotropy of these columns are not found directly in Cautun20. Instead these values, denoted by ∗, are calculated by applying the SHM and SHM^{++} DM models to the Cautun20 MW-mass distribution (see Sections 3.3 and 4.1 for further details).

Property	This work	Cautun20 + SHM∗	Cautun20 + SHM^{++}∗	Units
$\rho_\odot$	$8.5^{+1.6}_{-0.6}$	9.2	9.2	$10^{-3}\,M_\odot\,pc^{-3}$
	$0.32^{+0.05}_{-0.02}$	$0.34^{+0.02}_{-0.02}$	$0.34^{+0.02}_{-0.02}$	$GeV\,cm^{-3}$
$\sigma_{V,\odot}$	155^{+5}_{-6}	153∗	153∗	$km\,s^{-1}$
$\sigma_{V_r,\odot}$	162^{+9}_{-8}	153∗	170∗	$km\,s^{-1}$
$\sigma_{V_t,\odot}$	151^{+4}_{-5}	153∗	142∗	$km\,s^{-1}$
$\beta_\odot$	$0.14^{+0.06}_{-0.03}$	0 (isotropic)∗	0.3∗	–
$V_{Circ,\odot}$	231^{+8}_{-2}	230	230	$km\,s^{-1}$
$V_{Esc,\odot}$	554^{+12}_{-10}	549	549	$km\,s^{-1}$
M_{200}^{Total}	1.08	1.08	1.08	$10^{12}\,M_\odot$
M_{200}^{DM}	0.97	0.97	0.97	$10^{12}\,M_\odot$
$M_{200}^{Baryons}$	0.11	0.11	0.11	$10^{12}\,M_\odot$

VDFs have very similar forms to those previously discussed for the AU5 halo (see Fig. 9) and many of the conclusions reached for that example apply here too. In particular, we predict a small radial bias in the velocity anisotropy, $\beta_\odot = 0.14^{+0.06}_{-0.03}$, with the radial and tangential velocity dispersions being $\sigma_{V_r,\odot}^{MW} = 162^{+9}_{-8}\,km\,s^{-1}$ and $\sigma_{V_t,\odot}^{MW} = 151^{+4}_{-5}\,km\,s^{-1}$. These and other values are summarized in Table 1, where we also compare our results to those from the recent MW-mass model of Cautun20. In this table, the velocity dispersion's and anisotropy given for Cautun et al. are the results of applying the SHM with the parameters inferred from the Cautun et al. MW-mass model. See Section 3.3 for further details and discussion on the SHM.

The SHM is in good overall agreement with our inferred velocity distribution, although we find large fractional deviations in the high velocity tail of the distribution, the region to which DM direct detection experiments are most sensitive (Bozorgnia et al. 2019). The SHM model assumes an isotropic velocity distribution, at odds with the value of $\beta_\odot \sim 0.14$ in our model. As a result, the SHM does not perform as well when compared against the radial and tangential velocity distribution of our model.

We also give the predictions of the SHM^{++} model of Evans et al. (2019) in the fourth column of Table 1 and as the red dotted line in Fig. 11. This is an SHM model modified to include a secondary, highly radial distribution of DM, inspired by evidence that the MW experienced a strongly radial major merger in the past (Belokurov et al. 2018). Alongside a normal isothermal SHM velocity distribution, a fraction of the DM, $f_S \approx 0.2$, is modelled as a highly radial component, $\beta_{merger} \approx 0.9$, as an approximation of the contribution from the radial merger (see Evans et al. 2019 for further details). The resulting overall distribution has a radial anisotropy of $\beta_\odot^{++} = 0.3$, which is more highly anisotropic than any of our AURIGA haloes. While not explicitly split into separate distributions, the action distributions of our DM haloes reflect the accumulated merger history of each halo. Our analysis of these haloes suggests that, typically, DM haloes are inherently likely to have a slightly radially biased velocity distribution in the solar neighbourhood. Modelling individual contributions to the final DM

halo as separate distributions is an interesting possibility but is beyond the scope of this paper, and is left to future work.

5 CONCLUSIONS

We have used the AURIGA suite of hydrodynamical simulations of MW analogues to investigate the orbital distribution of DM particles in MW-mass haloes and to study how this distribution changes when including baryonic physics in the simulations. We have characterized the DM haloes in terms of the distribution of spherical actions: radial action, J_r, and angular momentum, L. We have studied these action DFs for all our relaxed haloes and have described how the actions can be used to (re)construct the density and velocity distribution of the simulated DM haloes. This can be achieved using an iterative method that, starting from a fixed baryonic distribution and an initial guess for the gravitational potential, constructs a DM halo density profile. At each step in the iteration the potential is updated from the DM mass profile obtained in the previous step until convergence is achieved.

The actions J_r and L are useful quantities for describing DM haloes since they are conserved during adiabatic changes (i.e. on long time-scales) in the gravitational potential. Many galaxy formation processes, although not all, are thought to be adiabatic and this suggests that haloes in DMO and Hydro simulations should have similar $F(J_r, L)$ DFs. This idea motivated us to investigate if indeed the action DF is conserved in the AURIGA suite between the DMO simulations and the simulations that include galaxy formation physics. We have found good agreement between the actions in the DMO and Hydro haloes, with differences at the $5 - 10$ per cent level. Most of these differences are due to statistical fluctuations; however, we also find systematic variations, with J_r being lower in the Hydro haloes. This difference in radial action leads to an ~ 8 per cent underprediction of the DM density profile when adiabatic contraction of a DMO halo is assumed. The J_r systematic difference is the same at all radii, suggesting that it is unlikely to be caused by effects associated with baryonic feedback which would mainly affect the central region of a halo.

If we know the $F(J_r, L)$ actions of a halo in a DMO simulation, we can predict the density and velocity profile of its counterpart in the hydrodynamical simulation with a precision of ~5 per cent (not withstanding the systematic effects discussed above). Most of the scatter is due to stochastic effects as well as to small deviations from the steady state assumption implicit in our method. This object-to-object scatter is a factor of 2 lower than for other methods, such as that of Cautun20. However, if we do not know the exact $F(J_r, L)$ distribution, we recover the density profiles only with ~15 per cent precision, with the major limitation being the halo-to-halo scatter in the action distributions.

We have illustrated the contraction of a DM halo in the presence of baryons by decomposing the halo into individual orbits of DM particles. The deeper potential in the Hydro case leads to a contraction, that is an inward shift, of the orbits. For a fixed orbital angular momentum, circular orbits contract the most while highly elliptical orbits contract the least. The DM halo is specified by the sum of all orbits as given by the $F(J_r, L)$ distribution. This property can be used to determine both the density and velocity distribution profiles of a halo.

We have applied our DM halo construction method to the halo of the MW. Starting from the $F(J_r, L)$ distribution of relaxed AURIGA Hydro haloes, in combination with the Cautun20 stellar and gas model of the MW and the value of the MW mass of Callingham19,

we have predicted the density and velocity distribution of our Galaxy's DM halo. This resulted in 17 models for the Galactic DM halo, which span possible DM distributions given the MW's baryonic component. We find good consistency between our inferred DM halo density and that inferred by Cautun20, and between the circular velocity curve predicted by our models and the one measured from *Gaia* DR2 data (Eilers et al. 2019). The consistency with the Cautun20 results provides an independent check that their DM halo contraction model gives a good description of the Galactic DM distribution.

A major advantage of our halo (re)construction method is that it can predict the velocity distribution of DM particles. We have tested this aspect of our method by comparing directly against measurements of the AURIGA haloes and found very good agreement. In particular, our method does better than the SHM at reproducing the high tail of the velocity distribution, a key input into direct DM detection experiments. We have applied the same analysis to the MW to predict the distribution of DM particle velocities and their components in the solar neighbourhood. Our results are in good agreement with the literature (e.g. Evans et al. 2019; Bozorgnia et al. 2019), and predict that the DM particles have a preference for radial orbits, with $\beta_\odot = 0.14^{+0.07}_{-0.03}$, and that the SHM overpredicts the high velocity tail of the velocity distribution. Furthermore, by using multiple action distributions, we have characterized the halo-to-halo scatter in the velocity distribution, which is important for understanding how robust are the constraints inferred from direct DM detection experiments.

A potential improvement to this work would be to extend the formalism to axisymmetric models, which provide a better description of disc galaxies such as the MW. In this case, the DM halo is described by the 3D action distribution, $F(J_R, L_z, J_z)$, where (R, z) denote the coordinates in the plane of the disc and perpendicular to it. (For an example of axisymmetric modelling, see Cole & Binney 2017.) As already discussed, the inner regions of DM haloes in hydrodynamical simulations are close to spherical, much more so than in their DMO counterparts, and within this work we have found no obvious correlation between the shape of the DM haloes and the results of our contraction method. We therefore expect the effects of including axisymmetry to be subdominant to the effects of halo-to-halo scatter.

Our work leaves open an important question: which baryon processes are responsible for the systematic difference in the action distribution between the DMO and the Hydro haloes? While such effects are small, about a few per cent, they produce a measurable effect on the density profile and velocity distribution. To overcame this systematic when modelling the MW, we have used the $F(J_r, L)$ distribution measured directly in the Hydro simulations. It remains to be seen if the same systematic deviations between DMO and Hydro haloes are present in other simulations and if the size of the effect varies between the various subgrid galaxy formation models implemented in different simulations.

In this work, when making predictions specifically for the MW, we employ a range of possible action DFs of an MW-mass halo as predicted by the AURIGA project. However, given the observations, for example the MW rotation curve, some distributions are more likely than others. This raises the question of which is the best-fitting $F(J_r, L)$ distribution for the MW, which we leave for future work. To address this will require modelling the still uncertain MW baryon mass distribution self-consistently alongside the DM distribution, since this is degenerate when predicting the inner ($\lesssim 50$ kpc) rotation curve (for details see Cautun20). Such a study is very worthwhile and timely, especially given the wealth of Galactic data available in the current and future *Gaia* DRs.

The method we have presented here provides a very comprehensive tool for modelling DM haloes in the presence of baryons and, furthermore, it can easily account for cosmological halo-to-halo variations in halo properties. In the age of precision MW astronomy, it is no longer possible to neglect the contraction of the Galactic DM halo or the diversity of DM distributions that form a halo. Our method provides an elegant and robust approach to incorporate these effects.

REFERENCES

Abadi M. G., Navarro J. F., Fardal M., Babul A., Steinmetz M., 2010, MNRAS, 407, 435
Abolfathi B. et al., 2018, ApJS, 235, 42
Arora A., Williams L. L. R., 2019, ApJ, 893, 53
Artale M. C., Pedrosa S. E., Tissera P. B., Cataldi P., Di Cintio A., 2019, A&A, 622, A197
Barnes J., White S. D. M., 1984, MNRAS, 211, 753
Belokurov V., Erkal D., Evans N. W., Koposov S. E., Deason A. J., 2018, MNRAS, 478, 611
Benitez-Llambay A., Frenk C. S., Ludlow A. D., Navarro J. F., 2018, MNRAS, 488, 2387
Bertschinger E., 1985, ApJS, 58, 39
Binney J., Piffl T., 2015, MNRAS, 454, 3653
Binney J., Tremaine S., 1987, Galactic Dynamics, Princeton University Press, Princeton, NJ
Blumenthal G. R., Faber S. M., Flores R., Primack J. R., 1986, ApJ, 301, 27
Bozorgnia N., Fattahi A., Frenk C. S., Cheek A., Cerdeno D. G., Gómez F. A., Grand R. J. J., Marinacci F., 2019, preprint (arXiv:1910.07536)
Burger J. D., Zavala J., 2019, MNRAS, 485, 1008
Callingham T. M. et al., 2019, MNRAS, 484, 5453
Cautun M. et al., 2020, MNRAS, 494, 4291(Cautun20)
Cole D. R., Binney J., 2017, MNRAS, 465, 798
Correa C. A., Schaye J., Wyithe J. S. B., Duffy A. R., Theuns T., Crain R. A., Bower R. G., 2018, MNRAS, 473, 538
Deason A. J., Belokurov V., Evans N. W., An J., 2012, MNRAS, 424, L44
Deason A. J., Fattahi A., Belokurov V., Evans N. W., Grand R. J. J., Marinacci F., Pakmor R., 2019, MNRAS, 485, 3514
Duffy A. R., Schaye J., Kay S. T., Dalla Vecchia C., Battye R. A., Booth C. M., 2010, MNRAS, 405, 2161

Dutton A. A. et al., 2016, MNRAS, 461, 2658

Eadie G., Jurić M., 2019, ApJ, 875, 159

Eggen O. J., Lynden-Bell D., Sandage A. R., 1962, ApJ, 136, 748

Eilers A.-C., Hogg D. W., Rix H.-W., Ness M. K., 2019, ApJ, 871, 120

Evans N. W., O'Hare C. A. J., McCabe C., 2019, Phys. Rev. D, 99, 023012

Fattahi A. et al., 2016, MNRAS, 457, 844

Frenk C. S., White S. D. M., Davis M., Efstathiou G., 1988, ApJ, 327, 507

Gaia Collaboration et al., 2018, A&A, 616, A1

Garrison-Kimmel S. et al., 2019, MNRAS, 487, 1380

Gnedin O. Y., Ceverino D., Gnedin N. Y., Klypin A. A., Kravtsov A. V., Levine R., Nagai D., Yepes G., 2011, preprint (arXiv:1108.5736)

Gnedin O. Y., Kravtsov A. V., Klypin A. A., Nagai D., 2004, ApJ, 616, 16

Grand R. J. J., Deason A. J., White S. D. M., Simpson C. M., Gómez F. A., Marinacci F., Pakmor R., 2019, MNRAS, 487, L72

Grand R. J. J. et al., 2017, MNRAS, 467, 179

Green A. M., 2010, J. Cosmol. Astropart. Phys., 2010, 034

Green A. M., 2017, J. Phys. G Nucl. Phys., 44, 084001

Han J., Wang W., Cole S., Frenk C. S., 2016, MNRAS, 456, 1003

Li Z.-Z., Jing Y. P., Qian Y.-Z., Yuan Z., Zhao D.-H., 2017, ApJ, 850, 116

Ludlow A. D., Navarro J. F., Angulo R. E., Boylan-Kolchin M., Springel V., Frenk C., White S. D. M., 2014, MNRAS, 441, 378

Ludlow A. D., Navarro J. F., Springel V., Vogelsberger M., Wang J., White S. D. M., Jenkins A., Frenk C. S., 2010, MNRAS, 406, 137

Ludlow A. D., Navarro J. F., White S. D. M., Boylan-Kolchin M., Springel V., Jenkins A., Frenk C. S., 2011, MNRAS, 415, 3895

Majewski S. R. et al., 2017, AJ, 154, 94

Mao Y.-Y., Strigari L. E., Wechsler R. H., Wu H.-Y., Hahn O., 2013, ApJ, 764, 35

McMillan P. J., 2011, MNRAS, 414, 2446

McMillan P. J., 2017, MNRAS, 465, 76

Navarro J. F., Frenk C. S., White S. D. M., 1996, ApJ, 462, 563

Navarro J. F., Frenk C. S., White S. D. M., 1997, ApJ, 490, 493

Navarro J. F. et al., 2010, MNRAS, 402, 21

Neto A. F. et al., 2007, MNRAS, 381, 1450

Piffl T., Penoyre Z., Binney J., 2015, MNRAS, 451, 639

Planck Collaboration XVI, 2014, A&A, 571, A1

Pontzen A., Governato F., 2012, MNRAS, 421, 3464

Pontzen A., Governato F., 2013, MNRAS, 430, 121

Posti L., Binney J., Nipoti C., Ciotti L., 2015, MNRAS, 447, 3060

Posti L., Helmi A., 2019, A&A, 621, A56

Power C., Navarro J. F., Jenkins A., Frenk C. S., White S. D. M., Springel V., Stadel J., Quinn T., 2003, MNRAS, 338, 14

Prada J., Forero-Romero J. E., Grand R. J. J., Pakmor R., Springel V., 2019, MNRAS, 490, 4877

Read J. I., 2014, J. Phys. G Nucl. Phys., 41, 063101

Sawala T. et al., 2016, MNRAS, 457, 1931

Schaller M. et al., 2016, MNRAS, 455, 4442

Schaye J. et al., 2015, MNRAS, 446, 521

Sellwood J. A., McGaugh S. S., 2005, ApJ, 634, 70

Somerville R. S., Davé R., 2015, ARA&A, 53, 51

Springel V., 2011, in Alves J., Elmegreen B. G., Girart J. M., Trimble V., eds, Vol. 270, Computational Star Formation. p. 203–206, IAU Symposium precedings

Tissera P. B., White S. D. M., Pedrosa S., Scannapieco C., 2010, MNRAS, 406, 922

Vasiliev E., 2019, MNRAS, 482, 1525

Vogelsberger M. et al., 2009, MNRAS, 395, 797

Wang W., Han J., Cautun M., Li Z., Ishigaki M. N., 2019, preprint (arXiv:1912.02599)

Watkins L. L., van der Marel R. P., Sohn S. T., Evans N. W., 2019, ApJ, 873, 118,

White S. D. M., Frenk C. S., 1991, ApJ, 379, 52

Zavala J., Frenk C. S., 2019, Galaxies, 7, 81

Zhu Q., Hernquist L., Marinacci F., Springel V., Li Y., 2017, MNRAS, 466, 3876

Zhu Q., Marinacci F., Maji M., Li Y., Springel V., Hernquist L., 2016, MNRAS, 458, 1559

APPENDIX A: RADIAL DISTRIBUTION OF ORBITS

Here, we describe how to construct the probability distribution that a particle on a orbit defined in terms of (J_r, L) is found at radial distance, r. We denote this radial probability distribution as $F(r|J_r, L)$. For simplicity, in the following we will work with the (E, L) actions (and thus calculate $F(r|E, L)$), which, given a gravitational potential, can be uniquely mapped to (J_r, L) space and vice versa (see the main text for details).

Consider an orbit defined by (E, L) in the potential $\Phi(r)$. The velocity components at r are defined as:

$$
\begin{aligned}
v|_r &= \sqrt{2(E - \Phi(r))} \\
v_t|_r &= L/r \\
v_r|_r &= \sqrt{v|_r^2 - v_t|_r^2},
\end{aligned}
\tag{A1}
$$

where for the radial velocity component we only consider its absolute value. A tracer on that orbit could have either negative or positive v_r depending on whether it is approaching or receding from the halo centre. The two points where $v_r = 0$ correspond to the peri- and apocentre of the orbit, r_{min} and r_{max}, with particles on the orbit spanning the radial range, $r_{min} < r < r_{max}$.

As described in the main text, the radial distribution of an orbit, either $F(r|E, L)$ or $F(r|J_r, L)$, is defined as the proportion of time an orbit spends at radial distance, r, normalized to unity. To calculate this, we first consider the amount of time, dt, taken by a test particle to travel from $r \rightarrow r + dr$. By Taylor expansion, we have

$$
r + dr = r + v_r dt + \frac{1}{2}\ddot{r}dt^2 + o\left(dt^3\right) ,
\tag{A2}
$$

where $\ddot{r}$ denotes the radial acceleration, that is the second derivative of r with respect to time. By neglecting dt^3 and higher order terms, we can solve for dt to obtain

$$
dt = \frac{-v_r + \sqrt{v_r^2 + 2\ddot{r}dr}}{\ddot{r}} .
\tag{A3}
$$

Away from the endpoints, $v_r^2 \gg 2\ddot{r}dr$ for small dr. Then $dt \approx dr/v_r$, that is the time spent at r is inversely proportional to the radial velocity component, as expected. As the test particle approaches the endpoints, $v_r \rightarrow 0$ and the radial acceleration terms can no longer be neglected. Then, the fraction of time spent at r, that is the radial distribution $F(r|E, L)$, can be written as

$$
F(r|E, L) dr = \frac{2}{T|_{E,L}} dt|_r ,
\tag{A4}
$$

where the factor of 2 accounts for the fact that a particle is found at the same r value twice along its orbit, that is once when approaching and once when receding from the halo centre. The normalization factor, $T|_{E,L}$, is the radial time period, which is given by

$$
T|_{E,L} = 2 \int_{r_{min}}^{r_{max}} dt|_r dr.
\tag{A5}
$$

To calculate $F(r|E, L)$, we use a radial grid with 1500 cells defined in the range $[0, 3R_{200}]$; this corresponds to a grid spacing, $dr = R_{200}/500 \sim 0.5$ kpc. Special treatment is required at the endpoints of the orbit where better spatial resolution is needed to track the orbit properly. The radial distribution and properties around 1 kpc of the endpoints of each orbit are then recalculated at a higher radial resolution of $dr^* = 5$ pc.

Averaged radial properties, such as the velocity dispersion or the velocity components, can be evaluated at a given radius using $F(r|J_r, L)$ as a weight. Any general orbital property depending on radius, $X(r)|_{J_r, L}$, can be calculated as

$$< X > (r) = \frac{1}{\rho(r)} \frac{M}{4\pi r^2} \int \int X(r)|_{J_r, L} F(J_r, L) dJ_r dL . \quad \text{(A6)}$$

APPENDIX B: SYSTEMATIC DIFFERENCES IN ACTION BETWEEN DMO AND HYDRO

Differences between DM haloes, such as in the $\rho(r)$, $\sigma(r)$, and $\beta(r)$ profiles, can be attributed to differences in their action distributions, $F(J_r, L)$. It is natural to expect that the greater the action difference, $\Delta_{(J_r, L)}$, between our DMO and Hydro haloes, the greater the difference in the contracted DM density profile. We explore this correlation in Fig. B1, which shows the integrated difference in the density profiles, $\Delta_\rho^{\text{total}}$, between the contracted DMO halo and the Hydro halo as a function of the difference in the action, $\Delta_{(J_r, L)}$, between the two haloes. In the relaxed halo sample, the $\Delta_\rho^{\text{total}}$ and $\Delta_{(J_r, L)}$ quantities are characterized by a small correlation of only 0.16. This suggests a complex relationship between action distributions and the physical halo. The relaxed sample has consistent differences of $\Delta_\rho^{\text{total}} \sim 8$ per cent ± 3 per cent, while the unrelaxed sample has a a wider scatter and a higher median $\Delta_\rho^{\text{total}} \sim 10_{-3}^{+10}$ per cent (a histogram of the results may be seen in the side panel of Fig. B1).

To better understand the effect of systematic differences in the $F(J_r, L)$ distribution between the DMO and Hydro simulations, we proceed to compare in Fig. B2 the radial profiles of several halo properties in the main text, when constructing the DM density profile given an $F(J_r, L)$ distribution, we find the self-consistent gravitational potential given the action distribution. However, differences in actions can lead to differences in potentials that would further
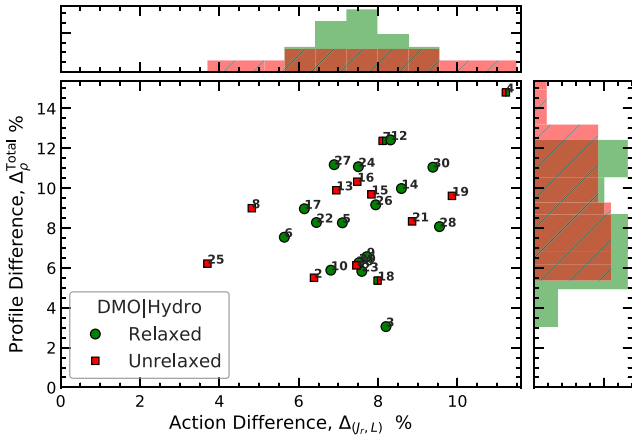

Figure B1. An exploration of the extent to which galaxy formation in the AURIGA suite is an adiabatic process. The *x*-axis show the difference in the action distributions, $\Delta_{(J_r, L)}$, of DM haloes between the DMO and corresponding Hydro simulations. An adiabatic process would conserve the action, i.e. $\Delta_{(J_r, L)} = 0$. The *y*-axis shows the integrated difference, $\Delta_\rho^{\text{total}}$, in the DM density profiles between the contracted DMO and the Hydro haloes. Each symbol represents one AURIGA system and the green circle or red square indicate if the halo is relaxed or unrelaxed. (See the text for definitions and further details.) In the relaxed sample, the $\Delta_{(J_r, L)}$ and $\Delta_\rho^{\text{total}}$ quantities show only a slight correlation (0.16), suggesting a complex relationship between differences in action distributions and differences in the final contacted profile.
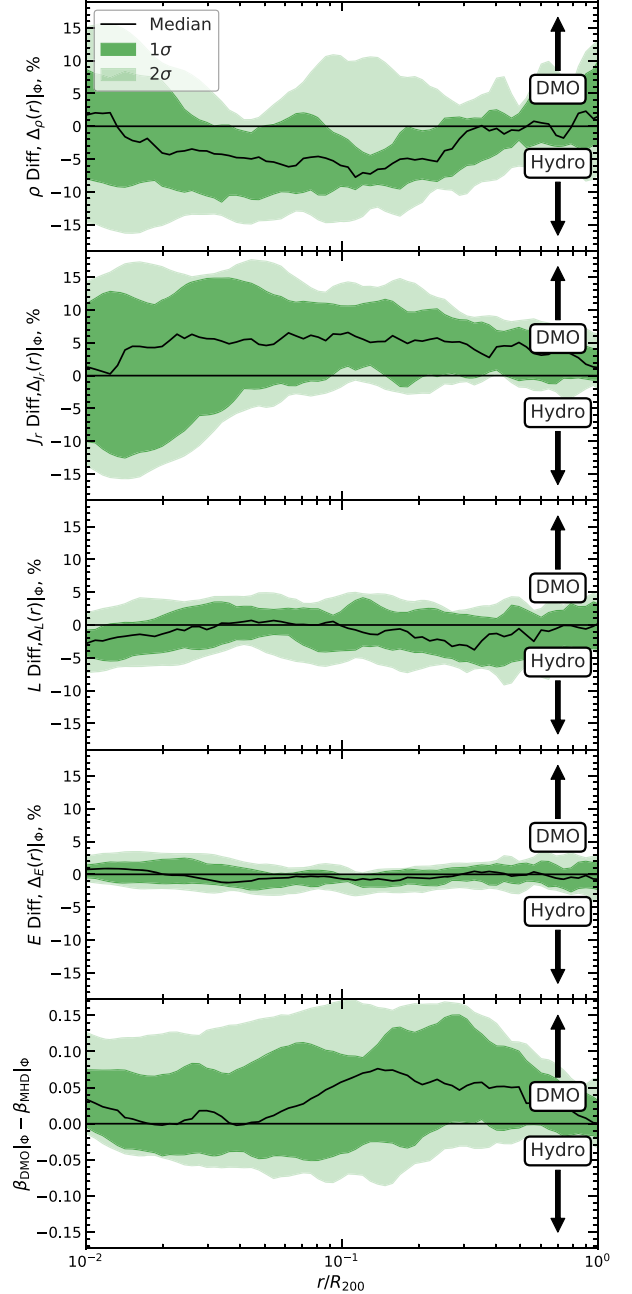

Figure B2. The fractional differences in selected halo properties as a function of radial distance. We plot the difference between halo quantities calculated using the $F(J_r, L)$ distribution measured in the DMO and in the counterpart Hydro simulation. When reconstructing the halo properties we use *the same fixed potential*, Φ_{Hydro}, measured in the Hydro simulation; in this way any difference in the plotted quantities are due to variations in the action distribution between the DMO and Hydro halo, and not to changes in the potential. We show, from top to bottom, the differences in the radial profile of: density, average radial action, average angular momentum, average energy, and average velocity anisotropy. The black line gives the median for our sample of relaxed AURIGA haloes, and the dark and light green regions the 68 and 95 percentiles, respectively. The DMO density profile, ρ (top panel), is systematically lower than in the Hydro counterpart, driven by a systematic suppression of radial action in the Hydro halo at every radius (second panel).

enhance differences in DM halo properties. To control for changes in potential, the results in Fig. B2 are obtained by constructing the DM haloes using the same fixed potential, Φ_{Hydro}, measured in the Hydro simulation. This allows a direct comparison of the orbital structure in physical space, providing insight into the dependence of the differences in density profile on the differences in action distributions. The potential mechanisms behind non-adiabatic effects can also be explored through the radial dependence of the action differences.

In Fig. B2, we consider the fractional differences in the density and average actions as a function of radius. In the top panel we see a ~ 5 per cent underprediction of the DM density when using actions of the DMO halo compared to the Hydro. The slightly changed potential generated with this density profile causes the density difference to grow with the iteration to $\Delta_\rho^{\mathrm{total}} \sim 8$ per cent in the final self-consistent profile. For L, we find very small systematic differences, but none the less the Hydro simulations tend to have slightly higher L values in the very inner regions and for $r \sim 0.3R_{200}$. In contrast, the energy distribution is characterized only by small stochastic differences.

The J_{r} in the DMO haloes is systematically higher at all radii away from the very centre $r \gtrsim 0.1R_{200}$ (second panel). For a single orbit, increasing J_{r} causes the median position of an orbit $<r>|_{\mathrm{Orbit}}$ to move radially outward, and mass to move from the radial centre of the orbit to its endpoints, as seen in Fig. 6. This effect across all orbits seems to drive the difference in density profile (top panel): the density is higher in the Hydro haloes at intermediate radii, but the density is higher in the DMO haloes at the centre and near R_{200}. The higher radial action gives more radial orbits in the DMO case, increasing β_{DMO} (see the bottom panel of Fig. B2).

For a discussion of how the results shown in Fig. B2 can be used to understand the effects driving the non-adiabatic change in DM actions between the AURIGA DMO and Hydro simulations, we refer the reader to the last paragraph of Section 3.2.

This paper has been typeset from a TEX/LATEX file prepared by the author.